nature communications

Article

https://doi.org/10.1038/s41467-024-54576-5

Hierarchically mimicking outer tooth enamel for restorative mechanical compatibility

Received: 19 February 2024

Accepted: 14 November 2024

Junfeng Lu[1,4], Jingjing Deng[2,4], Yan Wei[2,4], Xiuyi Yang[1,4], Hewei Zhao[1,4] ✉, Qihan Zhao[1], Shaojia Liu[1], Fengshi Li[1], Yangbei Li[1], Xuliang Deng[2] ✉, Lei Jiang[1,3] ✉ & Lin Guo[1] ✉

Tooth enamel, and especially the outer tooth enamel, is a load-resistant shell that benefits mastication but is easily damaged, driving the need for enamel-restorative materials with comparable properties to restore the mastication function and protect the teeth. Synthesizing an enamel analog that mimics the components and hierarchical structure of natural tooth enamel is a promising way to achieve these comparable mechanical properties, but it is still challenging to realize. Herein, we fabricate a hierarchical enamel analog with comparable stiffness, hardness, and viscoelasticity as natural enamel by incorporating three hierarchies of outer tooth enamel based on hierarchical assembly of enamel-like hydroxyapatite hybrid nanowires with polyvinyl alcohol as a matrix. This enamel analog possesses enamel-similar inorganic components and a nanowire-microbundle-macroarray hierarchical structure. It exhibits toughness of 19.80 MPa m$^{1/2}$, which is 3.4 times higher than natural tooth enamel, giving it long-term fatigue durability. This hierarchical design is promising for scalable production of enamel-restorative materials and for optimizing the mechanical performance of engineering composites.

Tooth enamel (especially the outer tooth enamel) plays a key role in resisting long-term complex external loads throughout a person's life; these external loads can generate tooth enamel damage and injure the entire tooth. Because mature tooth enamel is non-renewable and cannot undergo self-repair, enamel restoration has become a worldwide concern, and enamel-restorative materials are needed[1]. With respect to the functionality of tooth enamel, excellent comprehensive mechanical properties such as stiffness, hardness, and viscoelasticity serve as the important issues for enamel-restorative materials[2]. However, higher these mechanical properties are not necessarily better for tooth restoration[3]. Specifically, harder and stiffer materials than natural tooth enamel and those used for enamel restoration excessively abrase adjacent teeth[4,5], and softer materials can potentially lose their chewing ability to some degree because of the significant deformation under high loads[6]. Moreover, materials with insufficient viscoelasticity are not able to endure impact during chewing; this induces cracks within the material[7] and leads to the failure of the tooth restorative materials. Therefore, ideal enamel-restorative materials should possess comparable stiffness, hardness and viscoelasticity to those of natural tooth enamel. However, current commonly used tooth restorative materials, including metal, ceramic, and resins[8], fail to effectively address the problem due to the inherent mechanical limitations of these materials and the trade-off between stiffness and viscoelasticity[9].

The excellent mechanical properties of outer tooth enamel originate from its hierarchical structure, including both main column

---

[1]School of Chemistry, Beijing Advanced Innovation Center for Biomedical Engineering, Beihang University, Beijing, China. [2]Department of Geriatric Dentistry, NMPA Key Laboratory for Dental Materials, National Engineering Laboratory for Digital and Material Technology of Stomatology, Beijing Laboratory of Biomedical Materials, Peking University School and Hospital of Stomatology, Beijing, China. [3]CAS Key Laboratory of Bio-Inspired Materials and Interfacial Science, CAS Center for Excellence in Nanoscience, Technical Institute of Physics and Chemistry, Chinese Academy of Sciences, Beijing, China. [4]These authors contributed equally: Junfeng Lu, Jingjing Deng, Yan Wei, Xiuyi Yang, Hewei Zhao. ✉e-mail: zhaohewei@buaa.edu.cn; kqdengxuliang@bjmu.edu.cn; jianglei@mail.ipc.ac.cn; guolin@buaa.edu.cn

parallel arrangement and crystal hydroxyapatite (HA) with multiple amorphous phosphates[10]. Thus, replicating the hierarchical structure of outer tooth enamel is a feasible approach for overcoming the mechanical limitations and trade-off of man-made materials, making it mechanically suitable for enamel restoration[11]. Several strategies, such as layer-by-layer[7], ice-templated assembly[2], wet spinning[12], and biomimetic mineralization[13,14], have been developed to synthesize enamel-inspired materials. However, all presented enamel-inspired materials could mimic only one- or two-level hierarchies of the outer tooth enamel (at least three-level hierarchies for outer tooth enamel[11]). The mechanical properties of these materials indeed can overcome the mechanical limitations of traditional engineering materials, such as a ZnO-based film, addressing the trade-off between stiffness and viscoelasticity[7]; however, the exact stiffness, hardness, and viscoelasticity similar to outer tooth enamel is still unattainable due to the lack of a three-level hierarchy of outer tooth enamel that mimics a hierarchical nanowire–microbundle–macroarray arrangement and chemical gradients. Hence, mimicking the entire hierarchy of outer tooth enamel to achieve highly matchable mechanical properties remains challenging.

In this study, we successfully synthesized a hierarchical enamel analog (HEA) with the same hierarchical structure and similar inorganic components as that of outer tooth enamel using a sequential three-step strategy. As a result, the HEA possesses comparable outer enamel stiffness (84.3 GPa), hardness (3.9 GPa), and viscoelasticity (4.2 GPa) for restorative mechanical comparability, as well as outstanding toughness (19.8 MPa m$^{1/2}$) for long-term durability, showing great potential for enamel restoration. The outer enamel-like hierarchical structure and hierarchical fracture resistance contribute to the excellent mechanical performance of HEAs. This hierarchical design can facilitate a new path for synthesizing mechanically comparable enamel-restorative materials and mechanical property optimization.

Results

Structural and mechanical compatibility

The hierarchical structure of tooth enamel was first characterized and analyzed. At the millimeter scale, we found that tooth enamel shows gradients in the direction from the outer enamel to the inner enamel; here, the outer enamel mainly shows a parallel arrangement and the inner enamel mainly shows a decussation arrangement (Supplementary Fig. 1), resulting in the difference of mechanical properties (Supplementary Table 1). Since the outer enamel plays a key role in load bearing[15] and the stiffness and hardness are definitely greater than those of the inner enamel[16,17], we focused on biomimetic synthesis and analysis of the outer tooth enamel. The hierarchies of the outer tooth enamel can be defined at three levels: hydroxyapatite nanowires (HA, diameter of 30–40 nm) with an amorphous intergranular layer (AIP, thickness of 3–5 nm, first level); this consists of nonnegligible phosphates with diverse ions such as magnesium, iron, sodium and fluorine ions (Fig. 1d, and Supplementary Fig. 2)[18–20], nanowires that form the

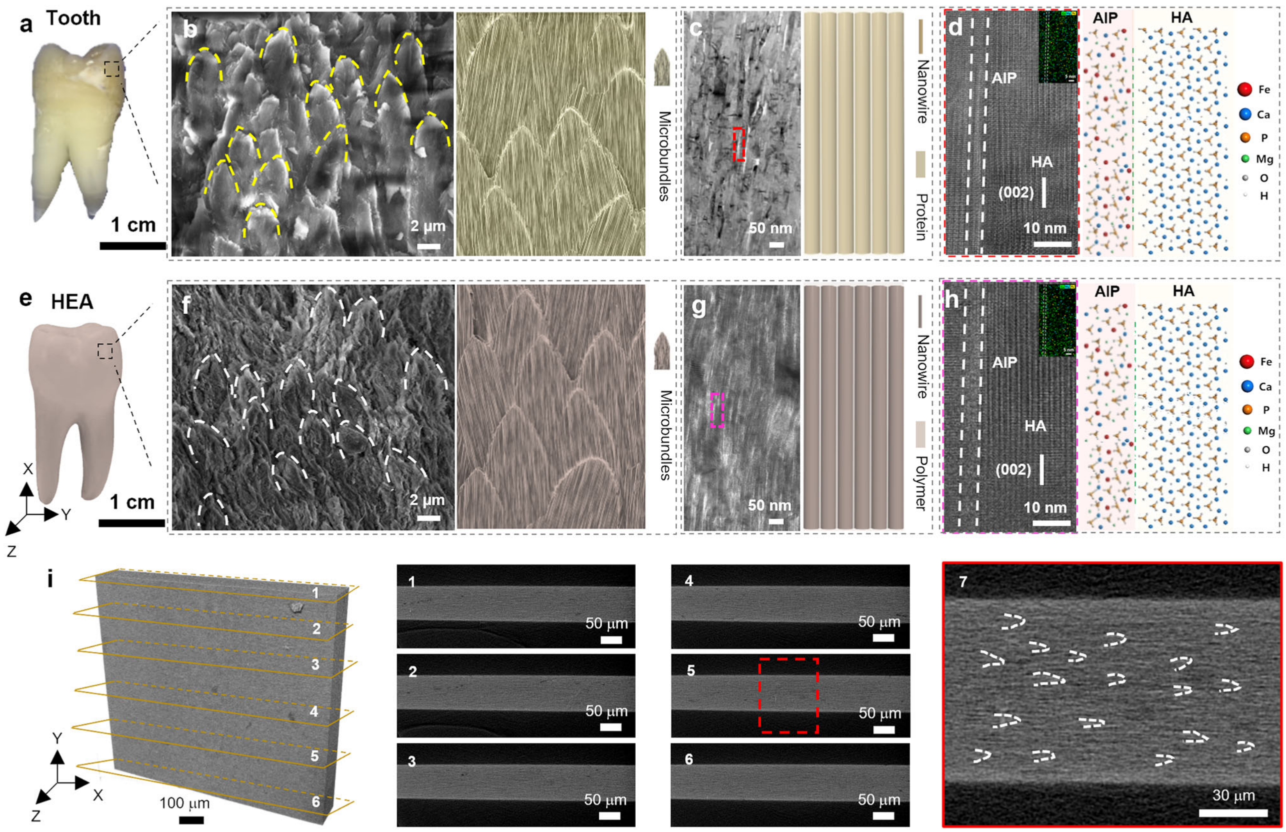

Fig. 1 | **Structure and mechanical properties of HEA. a** Optical photographs of the tooth enamel. **b** Scanning electron microscopy (SEM) image and structural schematic illustration of the enamel array as the yellow dashed curves shown in the SEM image. **c** Transmission electron microscopy (TEM) image and structural schematic illustration of the tooth enamel. **d** Magnified TEM image from the red zone in (**c**) with the corresponding structure schematic illustration. The results clearly showed the amorphous intergranular layer (AIP) on the surface of hydroxyapatite (HA) nanowires. Inset: Corresponding energy dispersive X-ray spectroscopy (EDS) map of (**c**). **e** Optical photograph of HEA. **f** SEM image and structural schematic illustration of the HEA array as the white dashed curves shown in the SEM image. **g** TEM image and structural schematic illustration of HEA. **h** Magnified TEM image from the pink zone in (**g**) with the corresponding structure schematic illustration. The results clearly showed the AIP on the surface of HA nanowires, which was consist with that of enamel. Inset: Corresponding EDS mapping of (**g**). **i** Nano-CT analysis of the HEA sample that presented the hierarchical structure of HEA in detail. **1-6**, Magnified nano-CT images from the slice of the bulk composite and **7**, enlarged nano-CT image from the red box zone in **5** (the white dashed curves showing the morphology of microbundles).

microbundles (diameter of 3–4 μm, second level, Fig. 1c), and microbundles that form the macroarray (thickness of 2 mm, third-level hierarchy, Fig. 1b)[21,22]. In addition, natural tooth enamel contains 2–3 wt.% water, which also influences its mechanical performance[23,24].

The hierarchical structure and outer enamel-like components of HEA are shown in Fig. 1e–h. HEA could be obtained at the macroscale and could be easily processed into a tooth-like shape by using computer-aided design and manufacturing (CAD/CAM) methods (Fig. 1e). The appearance of the HEA could be easily modified to a tooth-like state by a commonly used coloring and glazing processes; these results showed the feasibility of the HEA for potential clinical applications (Supplementary Fig. 3). The uniform macroarray structure of the HEA was identical to that of outer tooth enamel in terms of morphology (parallelly arranged microbundles) and size (diameter of ~3 μm) (Fig. 1b, f). These results showed the structural features of outer tooth enamel, with evidence of a biomimetic third-level hierarchy; moreover, similar results have not been successfully imitated in bulk materials. Close observation of the inner structure of the bundles in HEA (Fig. 1g) indicated that the HEA bundles were assembled from parallel-aligned nanowires 30–40 nm in diameter, similar to outer tooth enamel (Fig. 1c). The similarity at this scale of outer tooth enamel and HEA demonstrated that the second hierarchy of outer tooth enamel was also replicated. Based on an analysis of the nanowires in the HEA, the features of crystalline HA along the vertical direction, which were completely surrounded by an AIP layer with abundant Mg and Fe ions (thickness of 3 nm), were clearly present (Fig. 1d, h). These results were correlated to the main characteristics of the first-level hierarchy of outer tooth enamel. To analyzes the structural uniformity of the HEA, we performed nano-CT on the HEA and found that the hierarchical structure of the HEA was uniform across the entire sample (Fig. 1i). In addition, Fourier transform infrared (FTIR) spectroscopy, Raman spectroscopy, and X-ray photoelectron spectroscopy (XPS) characterization were performed (Supplementary Figs. 4–6), and the results from these techniques verified the chemical connections between the hybrid nanowires and oleic acid, with enamel-like bundles and polyvinyl alcohol (PVA), thus strengthening the interface rather than the physical connection between different components in HEA.

Tooth enamel is renowned for its high stiffness, hardness, and viscoelasticity, meaning that enamel is strong enough for chewing as well as high ability to dissipate energy generated by external loads. Recently, natural tooth enamel was found to possess porous elasticity, which also contributed to the creep behavior of enamel and the dissipation of energy in addition to the traditionally considered viscoelasticity[25,26] To evaluate the mechanical properties of HEA and outer tooth enamel and verify the comparability of them, we characterized enamel and HEA using nanoindentation with a load direction parallel to the nanowires, including both quasistatic (for stiffness and hardness) and dynamic mechanical analysis (DMA, for viscoelasticity). The Young's modulus (E), hardness (H), storage modulus (E'), and damping coefficient ($tan\delta$) were obtained (Fig. 2a–d, Supplementary Fig. 7). The average E and H values of the HEA were 86.2 ± 5.1 GPa and 3.8 ± 0.3 GPa, respectively; these results were consistent with those of natural enamel (84.3 ± 4.8 GPa and 3.9 ± 0.4 GPa) (Fig. 2a, b). Due to the equivalent stiffness and hardness, if damaged enamel was restored with HEA, the teeth would be sufficiently stiff to regain mastication function and avoid damage to the adjacent healthy tooth enamel; to note, these mechanical compatibilities are difficult to achieve with current enamel restorative materials. Moreover, the delamination strength of HEA and enamel is 3.5 folds larger than that of clinically used ZrO_2 and enamel (Supplementary Fig. 8), verifying the strong interface linking between HEA and the damaged tooth, which is essential for clinical restorative materials. As the tooth enamel and our biomimetic composites are anisotropic, we further measured E and H of the HEA, enamel and EA by nanoindentation with a load perpendicular to the nanowires; moreover, the E and H values obtained from different load directions were compared. We found that the E and H values of HEAs were similar to those of enamel tested in the same load direction, and the values obtained by the load parallel to the nanowires were the highest (Supplementary Fig. 9). Considering that the oral environment is humid, we further performed the nanoindentation test on HEA and enamel under water (Supplementary Fig. 10). Although the stiffness and hardness of HEA decreased slightly underwater compared with that of dry HEA, but the values were still high and comparable to those of enamel under water; as the stiffness and hardness of enamel also decreased under water (Supplementary Fig. 11, Supplementary Table 2). In addition, HEA exhibited specimen size-dependent mechanical response owing to its typical hierarchical structure; specifically, the stiffness and hardness of HEA decreased with the indenter contact diameter increasing, and these results were similar to those observed in enamel (Supplementary Fig. 12)[27,28].

Given that 10–15 Hz is typically regarded as the highest frequency that may occur during mastication in an oral environment[28], we firstly tested the dynamic mechanical properties of HEA and enamel at a dynamic frequency of 15 Hz. The HEA simultaneously exhibited high E' (68.7 ± 4.1 GPa) and $tan\delta$ (~0.061) values at a frequency of 15 Hz, similar to those of tooth enamel (67.9 ± 3.3 GPa and ~0.06, Fig. 2c, d). The viscoelasticity of the HEA (viscoelastic figure of merit, VFOM = $E'tan\delta$ = 4.2 GPa) far exceeded the limits (0.6 GPa) of artificially engineered materials (Supplementary Fig. 13 and Supplementary Table 3)[29]; these results contributed to its durability during potential engineering and dental restoration applications. We attributed this excellent viscoelasticity of the HEA to the hierarchical crack propagation generated by its hierarchical structure (Supplementary Fig. 14). Since common mastication events occur at a typical frequency of 1 to 2 Hz, we also conducted a dynamic nanoindentation test for HEA and enamel at the same frequencies. The E' and tan δ values of HEA were 68.3 GPa and ~0.072 at 1 Hz and 68.1 GPa and ~0.067 at 2 Hz, respectively (Supplementary Fig. 15); these results were comparable to the values at 15 Hz, implying that HEA possessed excellent viscoelasticity from low to high frequency for almost all kinds of occurring events. In addition, since the contact area of the tooth during mastication is 1–2 mm^2, larger than the contact area in nanoindentation DMA test, we further performed a macro-DMA test (contact area 4 mm^2) on the HEA and found that the viscoelasticity slightly decreased compared with that obtained by nanoindentation; however, the viscoelasticity was still outstanding (Supplementary Fig. 16).

To further understand the significance of the structural hierarchy on the mechanical performance, we synthesized other enamel-inspired composites without the complete hierarchy for comparison; here, one composite had a similar inorganic constituent as HEA but without the nanowire-to-microbundle hierarchical structure (defined as EA, Supplementary Fig. 17), and the other had the same hierarchy as HEA but without Mg or Fe in AIP (defined as HEA-Fe and HEA-Mg, respectively, Supplementary Figs. 18, 19). The mechanical properties (E, H, E', and tanδ) of all above-referenced materials were inferior to those of HEA (Supplementary Table 4), verifying the ability of the three-level hierarchy to mimic excellent mechanical properties.

Compared with clinical enamel restorative materials such as ceramics, alloys, and resins, as shown in Fig. 2f, g, and previously reported enamel-restoration materials, HEA is the first material that possesses simultaneous equivalent stiffness, hardness, storage modulus, and damping properties similar to those of natural tooth enamel. These comparable mechanical properties are vital for maintaining daily chewing function with long-term durability, without damaging adjacent teeth, making HEA promising for clinical applications.

Preparation and regulation

To precisely mimic the three-level hierarchy of outer tooth enamel, HEA was prepared through a combination of wet-spinning and magnetic-assisted dual-directional freeze-casting techniques, followed

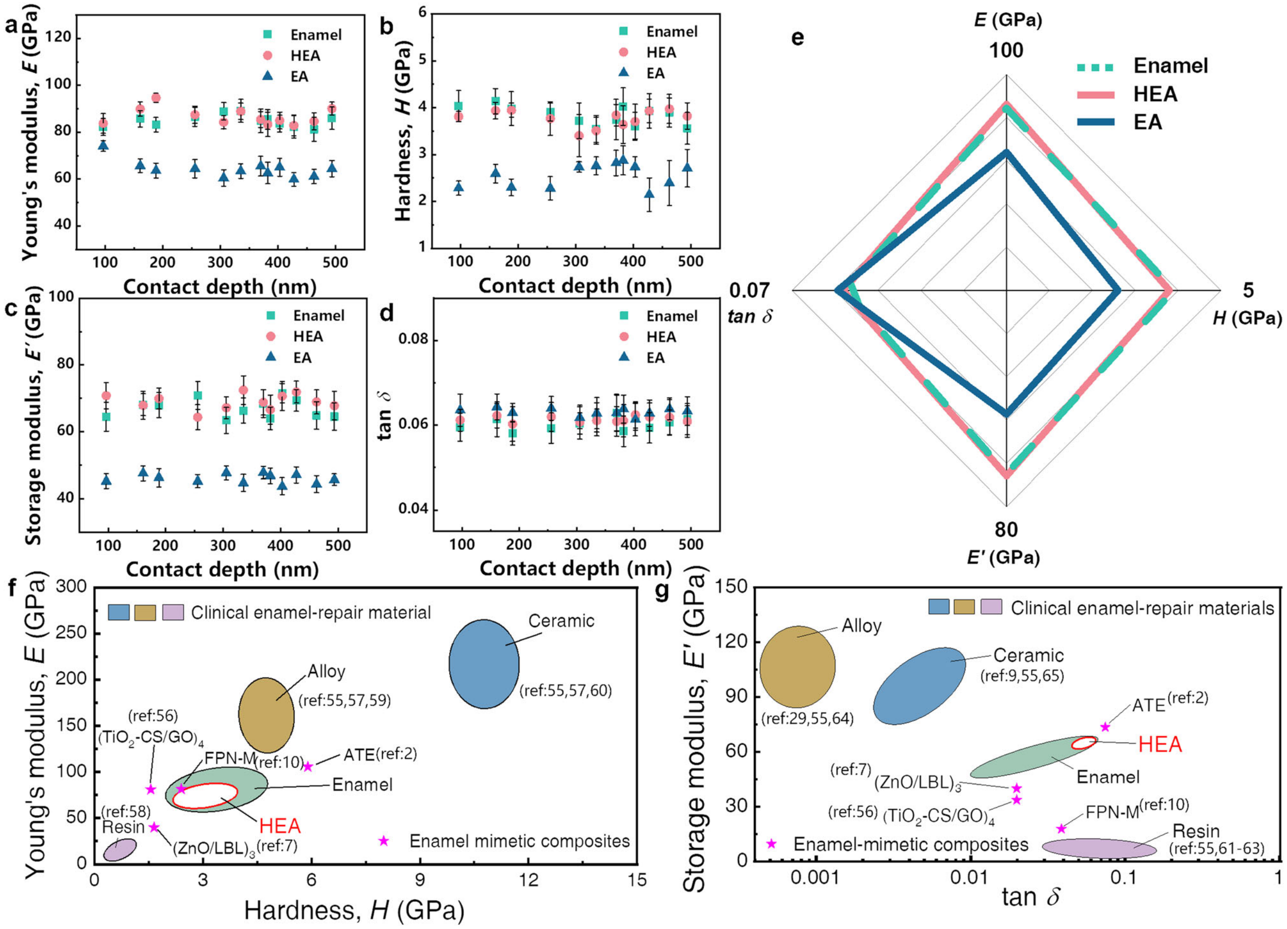

Fig. 2 | Mechanical properties of enamel, hierarchical enamel analog (HEA), and enamel analog (EA). The mechanical properties including, **a** Young's modulus (*E*), **b** hardness (*H*), **c** storage modulus (*E*′), and **d** damping coefficient (*tanδ*). The static nanoindentation tests (**a, b**) and dynamic nanoindentation (**c, d**) were measured under ambient conditions (25 °C, 15% RH) by a commercial TI 950 triboindenter (Hyistron) equipped with Berkovich diamond tips ($R = 100$ nm) along the direction of parallel to the nanowires (specimen size: 2–3 × 2–3 × 0.5–1.2 mm). Further details of this characterization can be seen in the "Method" (Nanoindentation section). Error bars represent standard deviation of more than 10 tests of each sample that were performed on at least three samples of enamel, HEA, and EA, respectively. **e** The comparison of mechanical properties between enamel, HEA, and EA. **f** The Young's modulus and hardness of HEA compared with those of enamel and clinically used tooth restorative materials and reference composites[2,7,10,55–60]. **g** The storage modulus and damping coefficient of HEA compared with those of clinically used enamel tooth restorative materials and reference composites[2,7,9,10,29,55,56,61–65].

by the synthesis of enamel-like HA nanowires with AIP. Specifically, uniform and enamel-like crystalline HA nanowires (Supplementary Fig. 20a) were first synthesized through hydrothermal method. To replicate the chemical gradient of the tooth enamel at the first hierarchy level, a thin amorphous magnesium and iron phosphate layer was coated on the HA nanowire surface (HA@Mg/Fe AIP) using a coprecipitation method (Fig. 3a, b). Mg and Fe were evenly distributed in the amorphous layer, and the thickness of this layer was ~3 nm (Fig. 3b–d, Supplementary Fig. 20b); this thickness was similar to that of outer tooth enamel. In addition, the amorphous layer was moderately chemically bonded to the HA nanowires (Supplementary Figs. 21, 22) to optimize the interface. The iron phosphate coating on the HA nanowire surfaces conferred the hybrid nanowires with paramagnetism (Fig. 3e)[30]. Second, parallel assembly of the hybrid HA@Mg/Fe AIP nanowires to form microbundles was achieved through wet spinning to mimic the second-level hierarchy (Fig. 3f). The presence of chain-like oleic acid homogenized the arrangement of hybrid nanowires and shear forces generated by flowing suspensions; this contributed to the parallel assembly of nanowires with oleic acid, strengthening the interface in the formed bundles[31]. Notably, the synchronization of the injection speed (0.5 mL min^{-1}) and volume ratio of ethanol (0.8) in the coagulation bath was vital for the formation of the microbundles with an ordered inner structure (Fig. 3g, Supplementary Fig. 23). The microbundles were ~3 µm in diameter with an ordered nanowire assembly structure and retained AIP (Fig. 3h, i; Supplementary Fig. 24); this was similar to outer tooth enamel at the second hierarchy level. Third, a magnetically assisted dual-directional freeze-casting method (Fig. 3j) was used to assemble the microbundles in parallel at the macroscopic scale, with PVA used as the organic matrix. The dual-directional freezing contributed to the parallel arrangement of these microbundles (Supplementary Fig. 25), and the presence of magnetism caused a more uniform arrangement of these microbundles on the skeleton on a large scale (Supplementary Fig. 26). After freeze-drying, we obtained a skeleton with oriented microbundles (Fig. 3k, l). We subsequently compressed the skeleton along the direction perpendicular to the bundles to obtain the final bulk dense composite, HEA; this process finished the entire hierarchy mimic (Fig. 3m, n).

Using the same strategy as above, HEAs with different distances between the microbundles were also produced by changing the ratio between the inorganic and organic components in HEA (1:1-5:1), with the inorganic nanowire content increasing from 45.94% to 77%; these were named HEA-1 to HEA-5 (Supplementary Fig. 27). These HEAs possessed various mechanical properties, including stiffness, hardness, and viscoelasticity (Supplementary Fig. 28), showing significant potential for the special design of tooth restorations in humans.

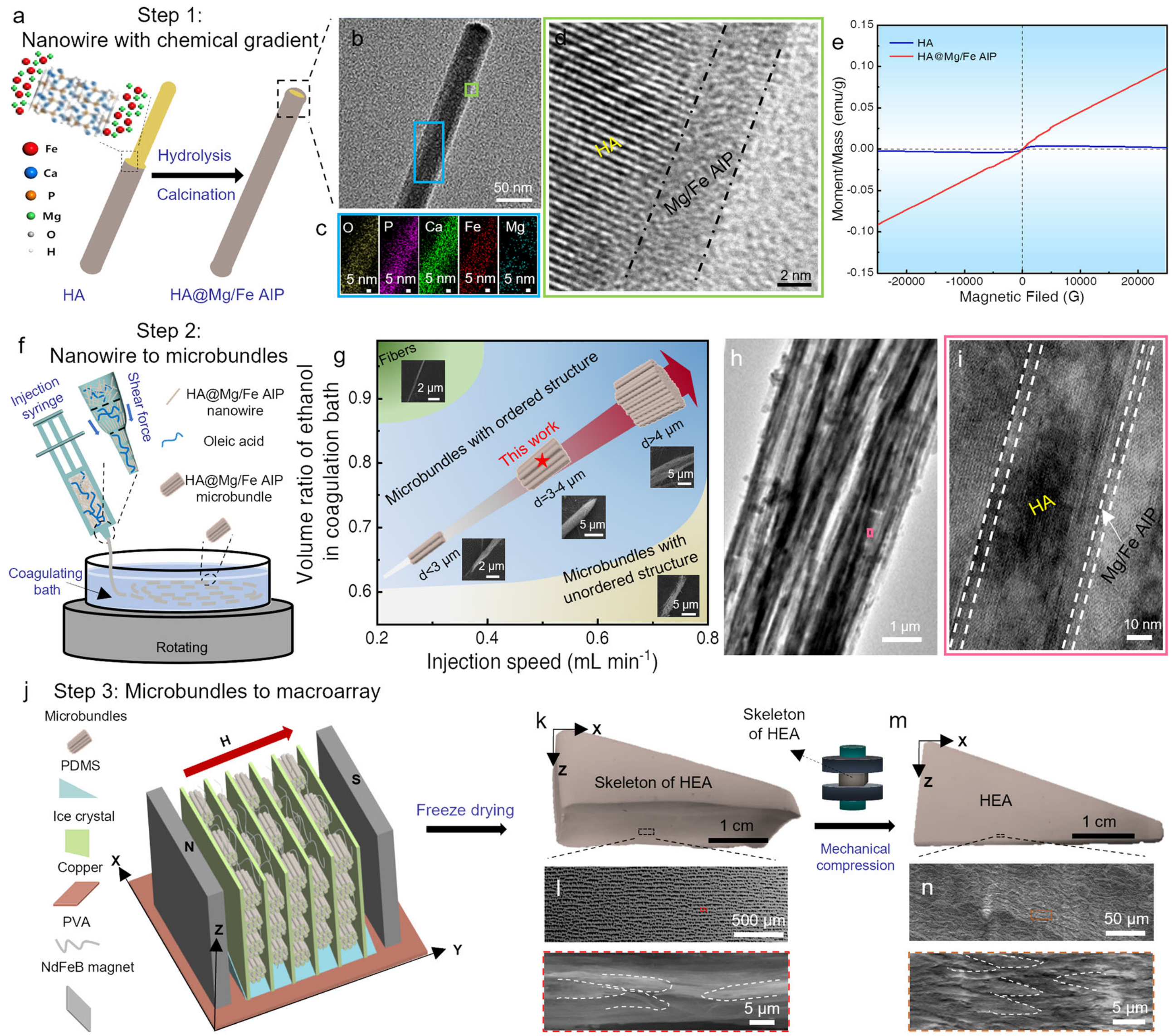

Fig. 3 | Strategy of HEA fabrication for mimicking the entire hierarchical structure of tooth enamel. **a** Schematic illustration of the first-level mimicking process. The HA@Mg/Fe AIP nanowires were prepared with the method of controlled metal ionic hydrolysis. Further details of this fabrication process can be seen in the Method (Synthesis of HA@Mg/Fe AIP nanowires section). **b** TEM image of the HA@Mg/Fe AIP nanowire. **c** Corresponding EDS map of the blue zone in (**b**). **d** Magnified TEM image from the green zone in (**b**). **e** Field-dependent hysteresis loops of the HA and HA@Mg/Fe AIP nanowires. The magnetic test was performed using PPMS-9 (Quantum Design, USA) with the system magnetic field of ±9 T at a scanning rate of 1-200 Gauss/s. Further details of this test can be seen in the Method (Material characterization section). **f** Schematic illustration of the second-level mimicking process, which was attained via wet spinning. The HA@Mg/Fe AIP microbundles were prepared with the method of controlling wet-spinning. Further details of this fabrication process can be seen in the Method (Synthesis of HA@Mg/Fe AIP microbundles section). **g** Effects of the injection speed and volume ratio of ethanol in the coagulation bath on the preparation of the wet-spinning product. The microbundles of different sizes in the figure were derived from controlled wet spinning method. The green region represented fibers, the yellow region represented microbundles with unordered structure and the blue region represented microbundles with ordered structure. Further details of this fabrication process can be seen in the Method (Synthesis of HA@Mg/Fe AIP microbundles section). **h, i** HRTEM images of the HA@Mg/Fe AIP microbundles. **j** Schematic illustration showing the third mimicry level. The macroarry was synthesized using magnetically assisted bidirectional freeze casting technique. Further details of this fabrication process can be seen in the Method (Preparation of HEA section). **k**, **l** Optical photograph and SEM images of the freeze-cast skeleton of HEA. **m**, **n** Optical photograph and SEM images of HEA. The white dashed lines indicated the morphology of microbundles.

Durability and biocompatibility

The durability and biocompatibility of HEA are vital factors that need to be addressed for the potential clinical applications of HEA. A cyclic contact fatigue test of HEA, enamel and EA at a frequency of 15 Hz (the highest contact frequency in the dental environment[32]) was performed with the load direction parallel to the nanowires to simulate oral contact (Fig. 4a)[33,34], and the typical indentation responses induced by the cyclic contact loading of these samples are shown in Fig. 4b. The three hysteresis loops showed the load–displacement curves for the first and last cycles of the loading history. For HEA, the last cycle (~150,000) corresponded to an increase in the maximum indentation depth of 155.7 μm with respect to the first cycle; this depth was far below that of EA and slightly lower than that of enamel. These results indicated that the HEA demonstrated strong resistance to external loads during long-term mastication simulations. The maximum displacement history over the entire contact fatigue life is shown in Fig. 4c. An inflection points at ~80,000 cycles was observed for the HEA curve, whereas those of enamel and EA were ~1000 and ~40,000, respectively; thus, HEA results in more occlusions without any evident changes, that are the flattest surface (Fig. 4d-i), the smallest roughness changes (Supplementary

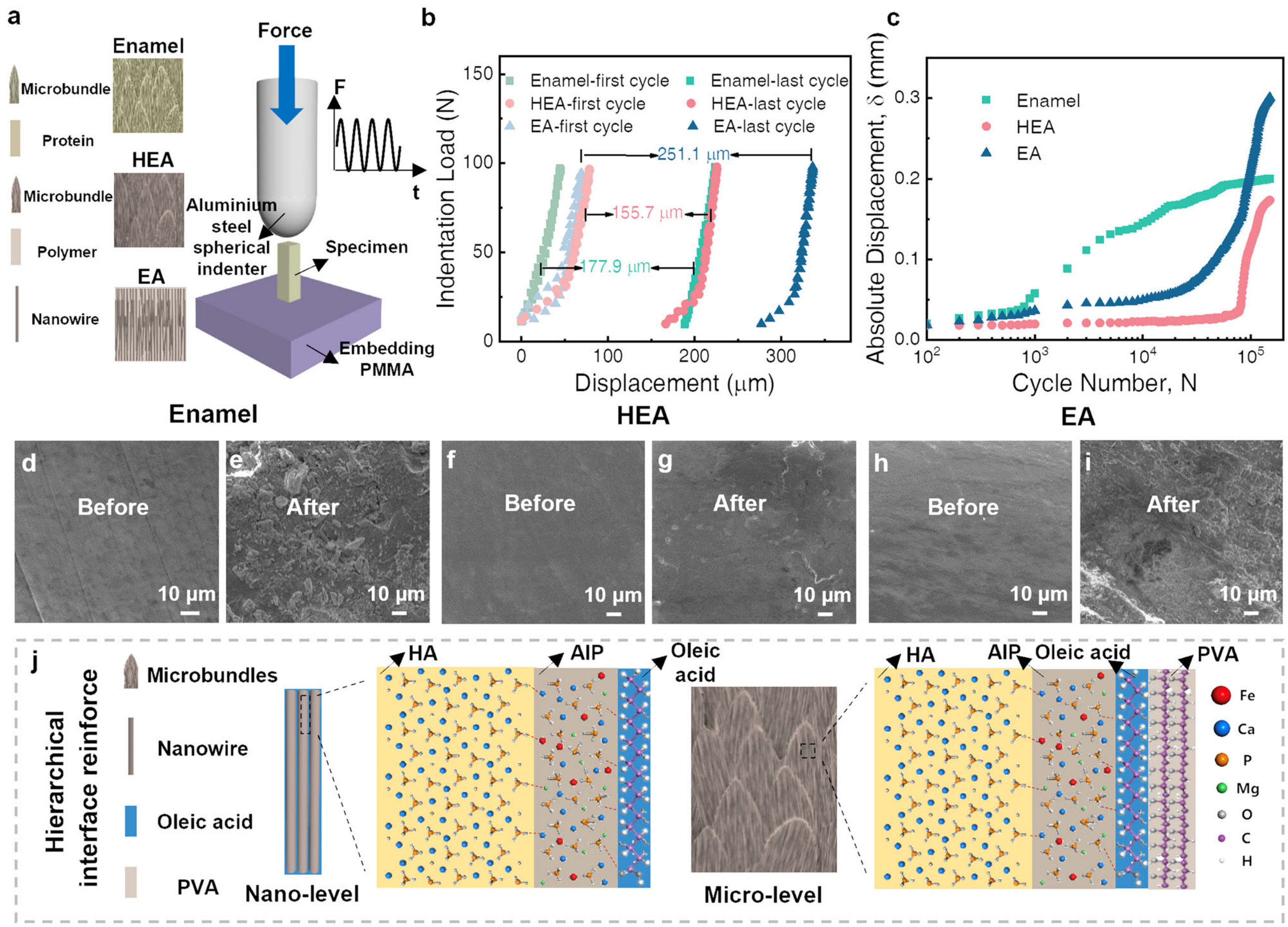

Fig. 4 | Comparison of the durability between enamel, hierarchical enamel analog (HEA), and enamel analog (EA). a Diagram of the cyclic fatigue test. The tests were performed on an electro-hydraulic servo fatigue test system at room temperature with a shinily spherical aluminum steel contact device (radius: 5 mm) at a frequency of 15 Hz, using a sinusoidal force of 0–98 N for 150,000 cycles (specimen size: 2 × 2 × 5–6 mm). All the tests were performed at least three times. Further details of this characterization can be seen in the Method (Cyclic contact fatigue test section). **b** Contact fatigue properties of tooth enamel, HEA and EA: evolution in the indentation displacement (δ) resulting from the cyclic contact test. The results are obtained from the above test methods. Further details of this characterization can be seen in the "Method" (Cyclic contact fatigue test section). **c** The displacement changes versus cycle number of enamel, HEA, and EA. The results are obtained from the above test methods. Further details of this characterization can be seen in the "Method" (Cyclic contact fatigue test section). **d-i** Morphology of the samples before and after the cyclic contact test. The surface of the HEA only showed more cracks, whereas the surfaces of the other two samples were broken; these results indicated the outstanding tolerance of the HEA during the simulated mastication process, which could be attributed to the existence of hierarchical and gradient structures, the effects of the organic and inorganic crosslinking and the strong confinement of the polymer chains providing strong support for the composite. **j** Schematic illustration of hierarchical interface reinforcement, showing the interaction of hydroxyapatite (HA, yellow area), amorphous intergranular layer (AIP, brown area), oleic acid (blue area), and PVA (gray area).

Fig. 29), lowest stiffness/hardness/viscoelasticity decay (Supplementary Fig. 30) and highest residual strength (Supplementary Fig. 31). Based on these data, HEA exhibited excellent mastication tolerance and fatigue properties, and its tolerances and properties were significantly better than those of the EA and slightly superior to natural tooth enamel; this showed the importance of the mimicked hierarchy, demonstrating the potential for long-term service in a complex dental load environment. In addition, we also performed contact fatigue tests of HEA and enamel using the same test conditions at a frequency of 1.5 Hz to evaluate the durability of HEA under the vast majority of oral application conditions (Supplementary Fig. 32); this frequency is the normal contact frequency in the dental environment. We found that the maximum indentation depth of HEA remained nearly constant during the 150000 cycles; these results showed the ultrahigh durability of HEA under normal conditions, similar to that of natural tooth enamel. In addition, the difference of the E values for enamel, EA, and HEA materials, which were obtained from the regions of the curves at initial unloading process and nanoindentation, respectively, also showing size-dependent effect (Supplementary Fig. 33).

Hierarchical interface reinforcement, including the nanolevel, and microlevel reinforcement, was also found to be vital for mastication tolerance and fatigue (Fig. 4j). Specifically, the hierarchical nanolevel interface consisted of two parts: one part is the HA–AIP interface with the coordination among Fe^{3+}, Mg^{2+}, P of PO_4^{3-}, and O of –OH (Supplementary Figs. 21, 22) and the other is AIP–oleic acid, which is likely associated with the chemical bonding of the metal ions and carboxyl groups (Supplementary Fig. 4). The hierarchical microlevel interface consisted of a PVA–oleic acid interface in addition to the above-mentioned interface (HA–AIP, AIP–Oleic), which resulted in hydroxy-carboxyl group interactions between PVA and oleic acid (Supplementary Figs. 4, 6). Thus, these suitable chemical bonds strengthened the interfacial connections among the nanowires, microbundles, and polymer matrix, improving the resistance against external loading during fatigue cycling.

Furthermore, a degree of sliding contact is always present during occlusion in the oral cavity, which also significantly leads to wear and associated damage to the loaded surface; therefore, we performed a toothbrushing wear test[35] and characterized the tested samples using

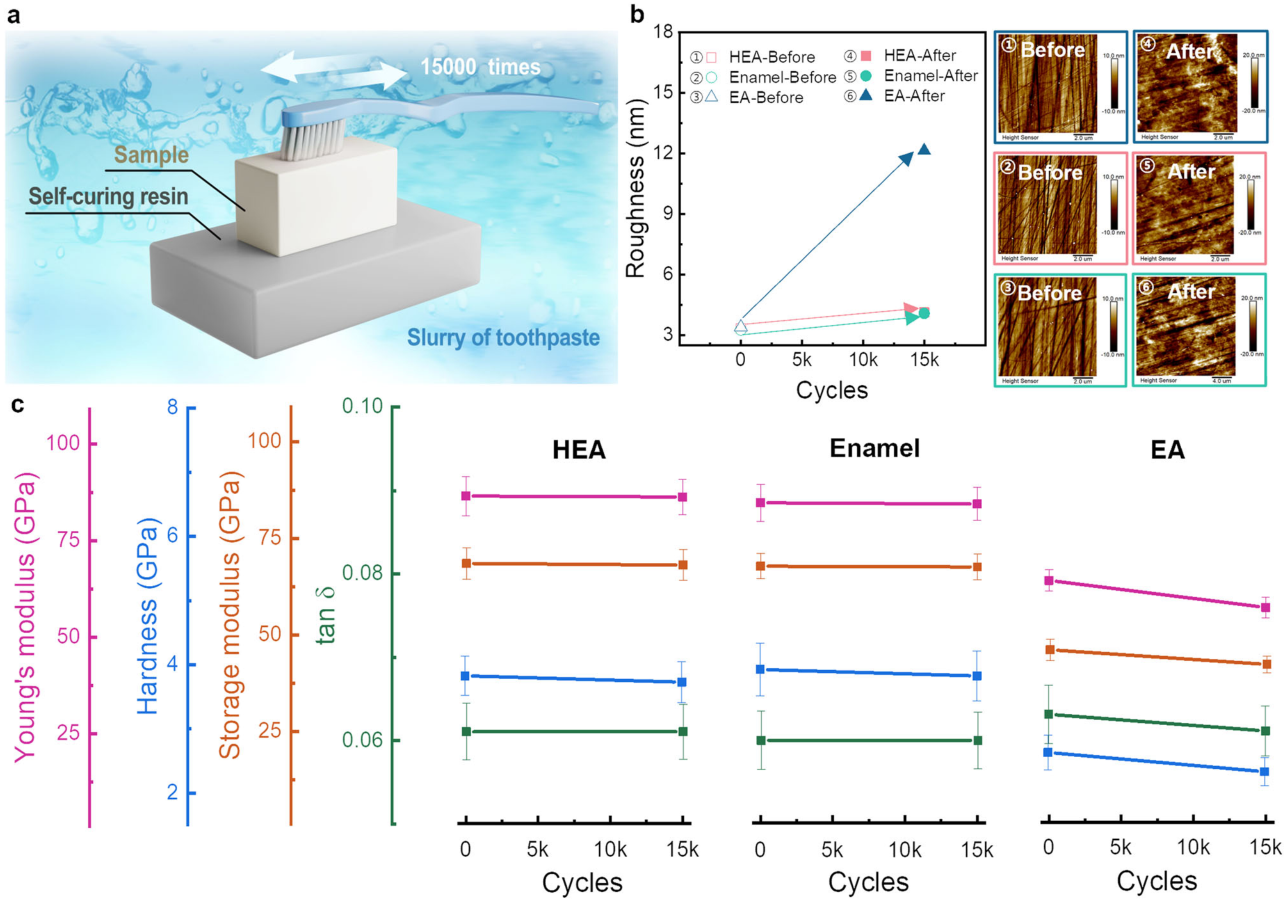

Fig. 5 | The results of toothbrush wear test. a Diagram of the toothbrush wear test. Specimens (10 × 2 × 2 mm) were fixed to the surface of each sample bench and a 200 g load was delivered by soft toothbrushes, all test samples were immersed in a slurry of toothpaste solution. All the tests were performed at least three times. Further details of this characterization can be seen in the Method (Toothbrushing wear test section). **b** The comparison of AFM analysis about EA, HEA, and enamel before and after toothbrushing tests. ①-⑥, The AFM images of EA, HEA, and enamel before and after toothbrushing tests, which are corresponding to the graph. The sample is fixed on the glass substrate, and the flat area is selected for AFM test. Further details of this characterization can be seen in the Method (Material characterization section). **c** Mechanical analysis of HEA, enamel, and EA before and after toothbrushing tests. The static nanoindentation and dynamic nanoindentation tests were measured under ambient conditions (25 °C, 15% RH) by a commercial TI 950 triboindenter (Hyistron) equipped with Berkovich diamond tips (*R* = 100 nm) along the direction parallel to the nanowires (specimen size: 2–3 × 2–3 × 0.5–1.2 mm). Further details of this characterization can be seen in the Method (Nanoindentation section). Error bars represent standard deviation of more than 10 tests of each sample that performed on at least three samples of HEA, enamel, and EA, respectively.

AFM and nanoindentation analysis (Fig. 5a–c). The mean square roughness of the tested HEA was ~4.13 nm, which was slightly higher than that of the original HEA (~3.35 nm) (Fi. 5b). This change was comparable to that observed in enamel (~3.27 nm to ~4.08 nm), and much more minimal than that of EA (~3.41 nm to ~12.14 nm). That is, the enamel-like hierarchical structure endowed HEA superior frictional resistance compared to the EA that without hierarchical structure, as the surface flatness of HEA showed only a small change (~0.78 nm) while EA exhibited a significant change (~8.67 nm). Moreover, Young's modulus, hardness, storage modulus and damping of HEA after the toothbrushing experiment were found to be ~85.4 GPa, ~3.7 GPa, ~68.2, and ~0.062, respectively (Fig. 5c). These values were nearly identical to those of the original HEA sample (~86.2 GPa, ~3.8 GPa, ~68.7 GPa, ~0.061), and this tendency was consistent with that observed in natural tooth enamel, indicating that HEA show outstanding wear resistance. In contrast, Young's modulus, hardness, storage modulus and damping of EA decreased by 15.6 %, 11.5 %, 8.3%, and 3.2 %, respectively, further demonstrated the significance of mimicking the hierarchal structure of enamel for HEA. Thus, HEA also exhibited outstanding longevity when the loading direction was perpendicular to the nanowires. The relatively low friction coefficient of HEA likely contributed to this excellent fatigue resistance with load perpendicular to the nanowires (Supplementary Fig. 34). Sum up, the HEA exhibited excellent durability under loads both parallel and perpendicular to the nanowires, covering the major loads occurring during the dental events, implying its potential for enamel restoration application.

To demonstrate the bio-performance of the HEA, the HEA and tooth enamel were cocultured with human gingival fibroblasts (HGFs); this experiment verified the good biocompatibility of the HEA (Supplementary Figs. 35, 36). In addition, the HEA demonstrated excellent antibacterial adhesion performance, as shown by bacterial adhesion tests of both the HEA and tooth enamel (Supplementary Figs. 37, 38 and Supplementary Table 5); these results strongly contributed to its long-term use in an oral environment[36,37].

High strength and toughness

The high strength and toughness contribute to the ability of materials to resist unexpected loads and prevent sudden damage, and these aspects are also vital for the durability of enamel restorative materials as well as more universal engineering applications[3,38,39]; therefore, we evaluated the flexural strength of the HEA through a three-point bending test, using EA and enamel as comparisons; these tests were all conducted with load perpendicular to the HA nanowires. The HEA demonstrated a high flexural strength of 159.6 ± 9.2 MPa and a fracture

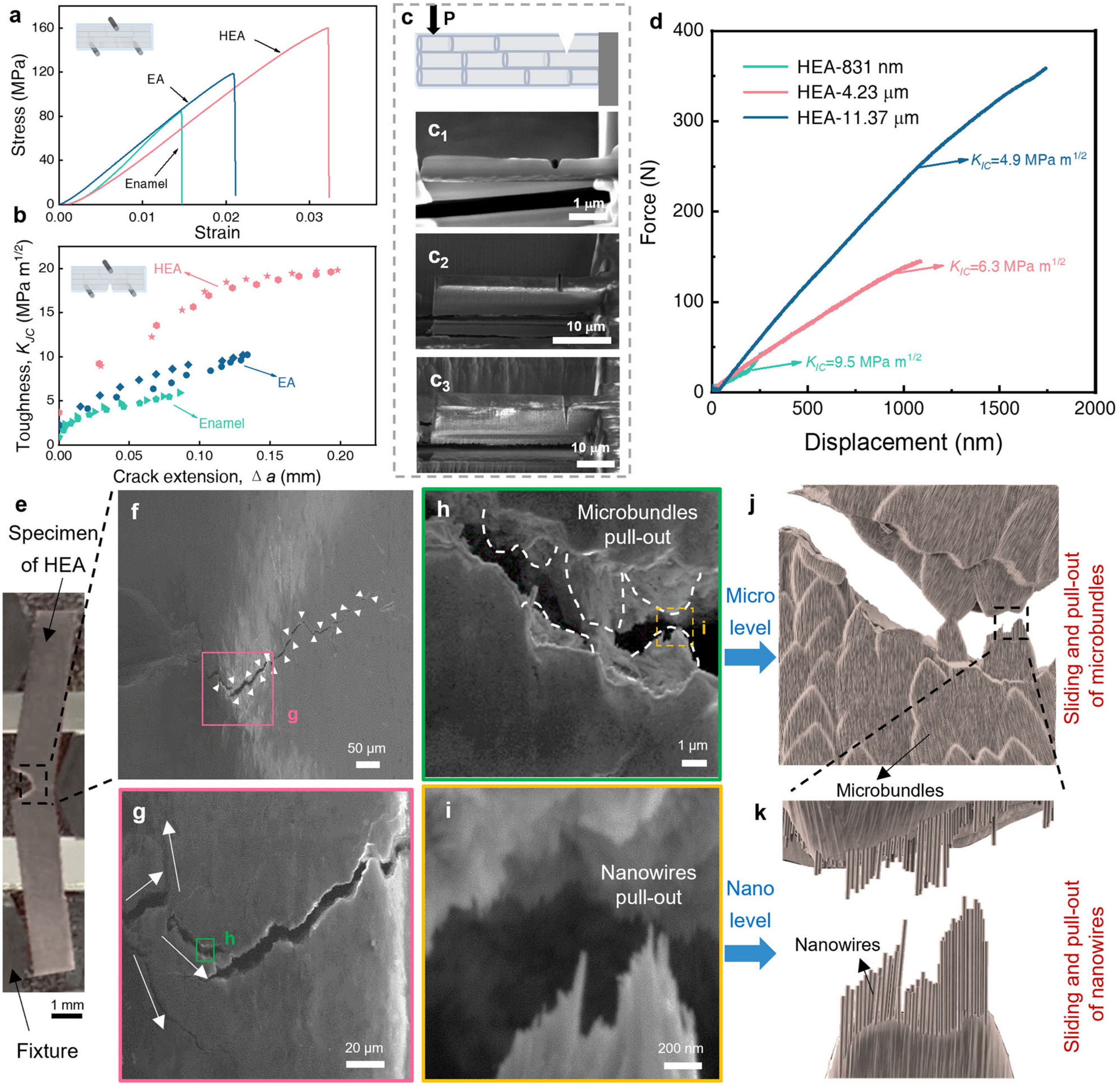

Fig. 6 | Fracture resistance properties of HEA. **a** Stress–strain curves measured by the three-point bending method for tooth enamel, HEA, and EA. Inset: The diagram of three-point bending test. The tests were measured with a Shimadzu AGS-X tester along the direction that perpendicular to the nanowires (Sample size: 15–20 × 1–2 × 0.5–1.2 mm for HEA and EA, 3 × 0.5–1 × 0.5–1 mm for enamel). All the tests were performed at least three times. Further details of this characterization can be seen in the Method (Three-point bending test and SENB test section). **b** Crack resistance curves (*R* curves) showing the resistance to fracture in terms of the stress intensity. Inset: The diagram of the SENB test. The SENB tests were also performed with a Shimadzu AGS-X tester along the direction that perpendicular to the nanowires (Sample size: 15–20 × 1–2 × 0.5–1.2 mm and a notch length of 0.4–0.6 mm for HEA and EA, 3 × 0.5–1 × 0.5–1 mm and a notch length of 0.1–0.2 mm for enamel). All the tests were performed at least three times. Further details of this characterization can be seen in the Method (Three-point bending test and SENB test section). **c** SEM images of single notch cantilever beam (obtained by FIB) of HEA-831 nm (**c$_1$**), HEA-4.23 μm (**c$_2$**), and HEA-11.37 μm (**c$_3$**). **d** The force–displacement curves for the in situ single notch cantilever beam test of HEA-831 nm, HEA-4.23 μm, and HEA-11.37 μm. The tests were conducted in an environmental scanning electron microscope equipped with an in situ mechanical test instrument (Hysitron PI-85) equipped with a flat diamond tip (5 μm in diameter). Further details of this characterization can be seen in the “Method” (Single notch cantilever beam tests section). **e** The optical photograph of the fracture HEA sample. **f** SEM image from in situ SENB tests. **g** Magnified SEM image from the pink zone in (**f**), revealing the crack branches. **h** Magnified SEM image from the green zone in (**g**). **i** Magnified SEM image from the yellow zone in (**h**). **j, k** Schematic illustration of the fracture process at microlevel and nanolevel, respectively.

strain of 0.032 ± 0.002; these were greater than those of EA and enamel (Fig. 6a, Supplementary Fig. 39). The fracture toughness of the HEA and reference materials were evaluated via single-edge notched beam (SENB) tests along the direction perpendicular to the microbundles, and typical force–displacement curves are displayed in Supplementary Fig. 40. The increase in toughness during stable crack propagation (K_{JC}) was evaluated by the *R*-curve effect[40,41] (Fig. 6b), which accurately reflects the toughness performance for engineering applications[42]. The K_{JC} of the HEA reached 19.80 ± 2.90 MPa m$^{1/2}$, corresponding to a 4.2-fold increase compared with initial crack initiation (K_{IC}, 3.79 MPa m$^{1/2}$); additionally, K_{JC} of the HEA was also 1.9 and 3.4 times greater than those of the EA and tooth enamel, respectively (Supplementary Fig. 41), demonstrating excellent cracking resistance during deformation. The strength and toughness of HEA-Fe and HEA-

Mg were also tested, and they were lower than those of HEA (Supplementary Table 4). The significant enhancement in toughness by the HEA compared with materials without the three-level hierarchy further demonstrated the importance of the hierarchical structure. Moreover, the strength and toughness of HEA under wet conditions were similar to those under dry environments, indicating the excellent stability of HEA (Supplementary Fig. 42).

HEA and enamel possess anisotropic structures; thus, their strength and toughness are also likely anisotropic. We further performed three-point bending and SENB tests on the HEA and enamel along the load direction parallel to the nanowires; here, the strength and toughness of both the HEA and enamel obtained in these parallel load directions were lower than those tested in the direction perpendicular to the nanowires, but the HEA values were still higher than those of the enamel obtained in the same load direction (Supplementary Fig. 43). This anisotropic mechanical performance of HEAs was consistent with those of other biomaterials with hierarchical structures, such as nacre[43]. The reason for the higher toughness of HEA compared with tooth enamel toughness might be due to the higher organic content of HEA and the use of PVA as a polymer with excellent toughness compared with protein in tooth enamel[44,45]. In addition, size-dependent mechanical properties are another characteristic of hierarchical materials. We prepared three single-notched cantilever beams of different sizes (one with a width of 831 nm containing several nanowires, one with a width of 4.23 μm containing one microbundle and one with a width of 11.37 μm containing several microbundles) via the focused ion beam (FIB) technique (Fig. 6c, Supplementary Table 6). Results showed that the value of K_{IC} generally decreases with an increase in specimen size. Specifically, HEA-831 nm showed the highest K_{IC} value of 9.5 MPa m$^{1/2}$, which is about 1.5 and 1.9 folds higher than that of HEA-4.23 μm and HEA-11.37 μm, respectively (Fig. 6d). Moreover, all the K_{IC} values of all three samples exceeded the initial crack toughness of bulk HEA materials (3.79 MPa m$^{1/2}$), indicating evident size dependence, and this phenomenon was similar to that of enamel[46].

Strength and toughness are considered mutually exclusive due to the conflict between intrinsic damage mechanisms and extrinsic toughening mechanisms[47]. To explore the underlying mechanisms for the combined high strength and toughness, the mechanical behaviors of HEAs were observed through in situ SENB tests by using an environmental scanning electron microscope (ESEM). The excellent strength and toughness were attributed to hierarchical fracture resistance (Fig. 6e-i), as shown in Fig. 6j, k. Specifically, when the samples were under load, the parallel microbundles slid against each other to dissipate energy, and the parallel nanowires inside the microbundles also slid against each other, absorbing additional energy and forming a unique hierarchical fracture resistance to bear the load. Therefore, this hierarchical resistance generated large-scale cracks (Fig. 6f) and reversed crack deflection (Fig. 6g), pulled out and interconnected microbundles (Fig. 6h) and nanowires (Fig. 6i); these extended the stable crack propagation route and dissipated energy to obtain excellent fracture toughness[38,42]. In addition, due to its hierarchical behavior under loading, HEA could endure large deformations, which could strongly prevent the sudden collapse of the HEA and promote its stability during mastication. In comparison, the EA had only one level of fracture resistance with small crack deflection (Supplementary Fig. 44).

Discussion

As previously stated, a three-step sequential strategy was proposed to mimic the three-level hierarchy of outer tooth enamel, namely controllable hydrolysis coating, wet-spinning, and magnetic-assisted dual-directional freeze-casting, resulting in the production of a bulk hierarchical enamel analog. The HEA exhibited comparable stiffness (84.3 GPa), hardness (3.9 GPa), and viscoelasticity (4.2 GPa) to those of natural tooth enamel (mainly outer tooth enamel, which plays a crucial role in mastication and tooth protection). This is due to the highly structural and compositional similarity between HEA and tooth enamel. Moreover, HEA exhibited excellent durability during contact fatigue tests and toothbrushing tests, even under conditions of extremely high-frequency and oral stress, which were even slightly superior to those observed in natural tooth enamel. This was due to the hierarchical interface reinforcement of nanolevel and microlevel, including the crystal/amorphous interface, organic/inorganic interface, and organic/organic interface. Additionally, the biological experiments demonstrated HEA is biocompatibility and exhibits antibacterial adhesion. Therefore, it can be concluded that the material has the potential for enamel restoration applications.

It is also noteworthy that HEA exhibited remarkable strength (159.6 ± 9.2 MPa) and toughness (19.80 ± 2.90 MPa m$^{1/2}$), which was originated from the unique hierarchical fracture resistance in the context of sliding and pull-out of nanowires and microbundles. Moreover, the strength and toughness of HEA can be enhanced to higher values (179.4 MPa and 26.90 MPa m$^{1/2}$, respectively) while only slightly reducing the stiffness and hardness of HEA by adjusting the organic/inorganic ratio (Supplementary Fig. 45). The exceptional combination of high strength and high toughness indicates that HEA has the potential for future applications in enamel restoration and may also be suitable for some engineering applications. To evaluate the mechanical advancements of HEAs, we make an overall mechanical comparison between HEAs and reference materials. The findings revealed that the toughness and flexural strength of the HEA were higher than those of natural materials, as well as previously reported HA-based materials (Fig. 7a, Supplementary Table 7), further implying the mechanical advantages of HEA for enamel restoration applications. In addition, the density of a material is an additional factor to be taken into account when selecting an appropriate one for engineering applications. Given the relatively low mass density of our fully dense HEAs (1.46–1.96 g/cm^3), a comprehensive comparison of HEAs with engineering materials was conducted, with specific strength and toughness calculated for each. The summarized plot demonstrated that the specific toughness of HEAs (15.2 MPa/m$^{1/2}$/(g/cm^3)) is the highest among engineering ceramics, polymers and metals, while the value of specific strength for HEAs (101 MPa/(g/cm^3)) was relatively high (Fig. 7b, Supplementary Table 8), further substantiating the superiority of the hierarchical design of HEAs and endowing HEA with potential applications for building materials, vehicles, aerospace etc.

Particularly, the structure of the inner and outer layers of tooth enamel is evidently distinct (Supplementary Fig. 1), indicating that the tooth enamel exhibits a gradient structure from the outer zone to the inner zone. Consequently, one unchanging objective of the study of enamel-like materials is to fully mimic the entire structure of a natural tooth enamel, including both the outer and inner zones, to achieve gradient mimic. Although this work did not construct a gradient structure akin to that of tooth enamel, we hypothesized that the synthesis of a material with an enamel-like gradient structure would represent another significant advancement in the field of enamel mimicry, leading to the development of unique mechanical performance. Accordingly, we endeavored to achieve an enamel-like structure gradient in an artificial tooth enamel (Supplementary Fig. 46) based on our proposed assembly strategy. The oriented nanowires with several lamellas were obtained by dual-directional freeze-drying and subsequently cross-stacked to realize the desired arrangement of nanowires. This preliminary experiment demonstrated the feasibility of our proposed strategy for the construction of a gradient in artificial composites and we will continue to pursue the development of a comprehensive enamel-mimicking material, encompassing both the outer and inner layers.

In summary, HEA displays considerable potential for utilization in enamel restoration and engineering applications in a lightweight form owing to its excellent and tunable mechanical properties, with the

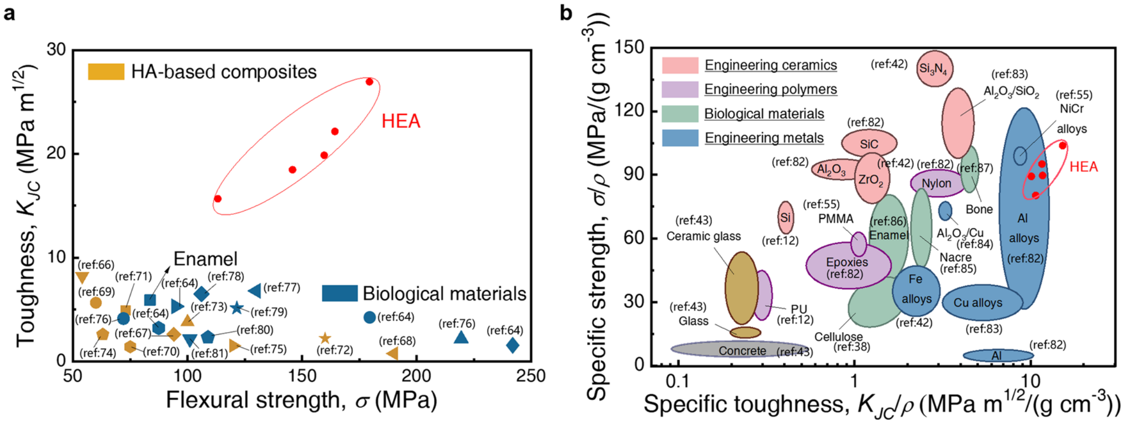

Fig. 7 | Comprehensive assessment of the fracture resistance properties for HEA. a The conflict between strength and toughness: fracture toughness versus flexural strength for HEA compared with biological materials and HA-based composites[64,66–81]. **b** Ashby chart of specific strength versus specific toughness for a range of engineering and biological materials[12,38,42,43,56,82–87]. PMMA, ZrO_2 and NiCr alloys are the clinical-used tooth restorative materials.

capacity to match and withstand the demands of these applications. And the well mimicking of the hierarchical structure related to the outer enamel may further facilitate the advancement of biomimetic tooth enamel materials.

Methods

Materials and reagents

NaOH, $CaCl_2$, $NaH_2PO_4{\cdot}2H_2O$, $FeCl_3$, and $MgSO_4$ were purchased from Aladdin Scientific Co., LTD (Shanghai, China). Oleic acid (tech. 90%), ethanol, $(NH_4)_2HPO_4$, and PVA (98–99% hydrolyzed, high molecular weight) were purchased from Alfa Aesar (USA). Polydimethylsiloxane (PDMS, M_w–4.8 kg mol^{-1}) was purchased from Beijing Xingde Precision Instrument Experimental Instrument Co., LTD (Beijing, China). And human erupted third molars, used in this study, were collected from patients aged between 18 and 40 years at Stomatology Hospital of Peking University after signing written informed consent. These are exempt from IRB approval. Only gender and age information were provided to the researchers.

Synthesis of HA nanowires

A hydrothermal method was adopted for the preparation of HA nanowires[48], as follows: NaOH aqueous solution (15 mL) was slowly added to a mixed solution dropwise with a 25 mL dropping funnel, which contained 10.5 mL oleic acid, 13.5 mL deionized water, and 6 mL ethanol in 250 mL beaker. After vigorously stirring for 30 min, aqueous solutions of 12 mL $CaCl_2$ (0.333 g) and 18 mL $NaH_2PO_4{\cdot}2H_2O$ (0.936 g) were successively added into the above mixture via a 25 mL dropping funnel drop by drop with a vigorously stirring (1000 r/min) of 30 min, respectively, to complete the ion exchange and eventually generate amorphous calcium phosphate precursor. Then, the as-prepared precursor suspension was transferred into a Teflon-lined stainless steel autoclave with a volume of 100 mL, solvothermal treated at 180 °C for 24 h, thus the crystalline hydroxyapatite nuclei forming and further growing into ultralong HAP nanowires. After cooling to room temperature, the mixture slurry was collected by centrifugation (7155 *g*), and washed with ethanol and deionized water followed by the alcohol wash (2 g NaOH dissolved in 200 mL ethanol). Finally, the centrifugal collection was freeze-dried for 48 h.

Synthesis of HA@Mg/Fe AIP nanowires

A method to control the hydrolysis of metal ions for the HA@Mg/Fe AIP nanowires was used inspired by our previous work[2]. Specifically, 0.053 g HA was added to a mixed solution consisting of 80 mL ethylene glycol and 20 mL deionized water in a 250 mL flask, and stirred (1000 r/min) for 30 min. Then, 0.0109 g $FeCl_3$, 0.1233 g $MgSO_4$, and 0.0111 g $CaCl_2$ were separately added to the above suspension and stirred vigorously (1000 r/min) for 30 min. Finally, 0.0264 g $(NH_4)_2HPO_4$ was added to the system and the system was then immersed in a water bath at 40 °C for 4 h under vigorous stirring (1000 r/min). The product was collected by centrifugation (7155 g), and washed three times with deionized water and subsequently freeze-dried for 48 h. Next, the dried samples were calcined at 300 °C for 2 h in a muffle furnace to obtain the target product, which was ultralong HA@Mg/Fe AIP nanowires. The HA@Mg AIP and HA@Fe AIP were similarly prepared according to the above methods except for the absence of $FeCl_3$ and $MgSO_4$, respectively.

Preparation of HA@Mg/Fe AIP bundles

A wet-spinning method was used for the preparation of HA@Mg/Fe AIP bundles based on the research[49]. Briefly, 5.5 mL oleic acid, 7.5 mL deionized water and 2 mL ethanol as well as 90 mg HA@Mg/Fe AIP nanowires sample were mixed in a 25 mL beaker with vigorously stirred (1000 r/min). After that, 7.5 mL NaOH (0.1 g) aqueous solution in a 15 mL beaker was slowly added to the above solution dropwise via a 15 mL dropping funnel. Then, the as-prepared suspension was transferred into a Teflon-lined stainless steel autoclave with a volume of 50 mL, treated at 180 °C for 12 h, followed by vigorously stirring (1000 r/min) for 30 min. After the autoclave cooled down to room temperature, the slurry at the bottom was collected for further use. Then a 1 mL injection syringe was used for continuously spinning the slurry into the rotating (30 r/min) coagulation bath at a speed of 0.5 mL min^{-1}, and standing for 5 min. The coagulation bath contained 80 vol% ethanol and 20 vol% water. Finally, the bundles were collected by centrifugation (7155 *g*) and subsequently freeze-dried for 48 h. The HA@Mg AIP and HA@Fe AIP bundles were similarly prepared according to the above methods via HA@Mg AIP and HA@Fe AIP nanowires.

Preparation of HEA

Enamel-like aligned lamellar composites were prepared by magnetically assisted bidirectional freeze casting of HA@Mg/Fe AIP bundles with PVA slurry above a polydimethylsiloxane (PDMS) wedge on a cooling stage. Briefly, 0.21 g PVA was fully dissolved in 7 mL deionized water within a 20 mL beaker in a water bath at 80 °C under vigorous stirring (1000 r/min). After, various amounts of HA@Mg/Fe AIP bundles (HA@Mg/Fe AIP bundles/PVA = 1:1 to 5:1, mass ratio) were added to the PVA solution with vigorously stirring (1000 r/min) for 48 h at room temperature. The slurry was subsequently injected into a Teflon mold (40 × 20 × 30 mm) with a PDMS wedge (25°) as the bottom with the addition of 2.1 mg glutaraldehyde (GA, Aladdin). Additionally, a magnetic field gradient was applied using the edge of a 60 mm × 10 mm × 40 mm rare earth magnet (Sintered NdFeB magnet, N35, China) placed parallel to the Teflon mold along the long axis. And the whole reaction unit was placed on the top surface of a T-shaped copper cylinder (size: 200 × 30 × 5 mm, and the pillar is 5 × 30 × 100 mm), while the lower surface was immersed in a liquid nitrogen reservoir. During the freezing process, lamellar ice crystals grow in parallel due to the double temperature gradient. At the same time, the HA@Mg/Fe AIP bundles in the slurry were ejected from the generating solidification front and arranged in parallel to each other between the ice layers. Frozen samples were sublimated for more than 48 h, followed by room temperature compression at 30 MPa for 2 h using an adapted cast steel die.

The reference HA-based composite (EA) was synthesized according to the same strategy as above, using the HA@Mg/Fe AIP nanowires as nanoscale blocks instead of HA@Mg/Fe AIP bundles. The other two HA-based composites based on HA@Mg AIP and HA@Fe AIP bundles were prepared as the contrast, named as HEA-Mg and HEA-Fe, respectively.

Preparation of the gradient enamel-inspired composite

The gradient enamel-like composite was prepared by magnetically assisted freeze casting of HA@Mg/Fe AIP nanowires with PVA slurry above a PDMS flat base on a cooling stage. Briefly, PVA (0.21 g) was fully dissolved in deionized water (7 mL) in a water bath at 80 °C. After that, 1.05 g HA@Mg/Fe AIP nanowires were added to the PVA solution vigorously (1000 r/min) stirring for 48 h at room temperature. Then, the slurry was injected into a Teflon mold (40 × 20 × 30 mm) with a PDMS flat base as the bottom with the addition of 2.1 mg glutaraldehyde. Additionally, a magnetic field was applied using the edge of a 60 mm × 10 mm × 40 mm rare earth magnet placed parallel to the Teflon mold along the long axis. The whole reaction unit was placed on the top surface of a T-shaped copper cylinder (size: 200 × 30 × 5 mm, and the pillar is 5 × 30 × 100 mm), while the lower surface was immersed in a liquid nitrogen reservoir. Frozen samples were sublimated for more than 48 h, then the skeleton was obtained. Secondly, three skeletons were stacked from bottom to top, and the two adjacent frames were rotated 90° clockwise. A thin layer of high-viscosity PVA solution was applied between the adjacent frames as the interlayer binder. Then the whole sample system was mechanically compressed using an adapted cast steel die and densified (80 °C, 30 MPa, 2 h) to obtain the gradient enamel-inspired composite with three layers.

Material characterization

The morphology of all the samples mentioned in the work was characterized with SEM (JEOL-7500F). The surface constituents were analyzed by EDS (Oxford, INCA Energy 250). The TEM images were obtained with a JEOL JEM-2100F at an accelerating voltage of 100 kV. The slicing specimens of HEA were cut using a focused ion beam (FIB, Helios NanoLab 460HP) and the scanning transmission electron microscopy—high-angle annular dark field of the sliced specimens were obtained with FEI G2 at an accelerating voltage of 200 kV. X-ray diffraction (XRD) analysis were was performed using a SHIMADZU XRD-6000, with a scan range from 10° to 80° and scan rate of 5°/min. FTIR was performed using a Thermo Nicoletnexus-470 FTIR instrument. Raman spectroscopy measurements were carried out using a LabRAM HR800 (Horiba JobinYvon) with an incident laser with 514 nm wavelength. All of the XPS measurements were taken in an ESCALab220i-XL (Thermo Scientific) using a monochromatic Al KR X-ray source. Thermogravimetric analysis was performed with NETZSCH TG 209F3 at an airflow rate of 10 °C/min. A water contact angle tester (Kruss DSC100, Germany) was used to test the water contact angle of different samples. The Zeta potential was measured on the surface of the sample using a Zeta potentiometer (Malvern Instruments, Worcestershire WR, UK). The samples for atom probe tomography analysis were cut by FIB (FEI, Helios 600) according to the standard protocol[50]. We used the Cameca LEAP 3000X HR with a picosecond-pulse high-voltage laser (pulsing mode at 15% pulse fraction) and the target evaporation rate was controlled at 4 ions for 1000 pulses to further determine the structure of tooth enamel. The specimen temperature was maintained at 80 K and the test vacuum pressure was ~2.5×10^{-11} torr. The data processing and three-dimensional reconstruction were performed using the CAMECA integrated visualization and analysis software IVAS 3.8.8. The different surface roughness of enamel was reviewed using atomic force microscopy (AFM) (Bruker Dimension Icon), where specimens were pasted on steel disks. And the AFM operation in the air was conducted to image the initial morphological state of the samples. Specifically, the sample is fixed on the glass substrate, and the flat area is selected for AFM test, which is carried out on the Dimension Icon AFM machine (Bruker, USA) equipped with a probe of Scanasyst air model at a scan rate of 1 Hz. The nano-CT analysis was performed as followed: In this experiment, Bruker Skyscan1272 in Germany was used. The X-ray source and detector were placed on both sides of the turntable respectively. Conical X-rays penetrated the samples placed on the turntable and were received by the detector. The samples could be translated horizontally, vertically, and vertically to change the scanning resolution. After each rotation of a tiny angle, the projection map is obtained from the X-ray irradiation sample, and the series of column projection maps obtained after the rotation of 360° are mapped and reconstructed in three dimensions. The magnetic test was performed using PPMS-9 (Quantum Design, USA) with the system magnetic field of ±9 T at a scanning rate of 1–200 Gauss/s. The testing temperature was 1.9-400 K with a scanning speed of 0.01–12 K/min.

Nanoindentation

The stiffness of different samples was measured under ambient conditions (25 °C, 15% RH) by a commercial TI 950 triboindenter (Hyistron) equipped with Berkovich diamond tips (R = 100 nm, 200 nm), a square tip (500 nm) and a spherical tip (1 μm) using a continuous depth-sensing indentation technique along the direction of parallel and perpendicular to the nanowires. If there is no specific discussion, the tips for nanoindentation are Berkovich diamond tips (R = 100 nm). The peak force and load time were set at 10,000 μN and 10 s for quasi-static nanoindentation, at 200 mN and 20 s for high-load quasi-static nanoindentation, the hardness and Young's modulus were calculated following the methods of Oliver–Pharr[51]. For the dynamic mechanical analysis (DMA) experiment, samples were loaded to a maximum force of 10,000 μN from 20 μN at a frequency of 15 Hz and an initial dynamic force of 20 μN. All specimens were cut with a water-cooled, low-speed diamond saw with a size of 2–3 × 2–3 × 0.5–1.2 mm.

In accordance with the methodology employed for the nanoindentation tests conducted in aqueous environments, the samples were positioned within a holder that could be filled with water, thus ensuring that the sample was completely submerged and surrounded by a thin layer of water on all sides, and then the tests were performed using the identical loading method as that employed for the dry samples with a diamond tip (R = 100 nm) immersed in water.

Macroscopic dynamic mechanical analysis test

Samples with dimensions of 2 mm × 2 mm × 5 mm were mounted on a dynamic thermomechanical analyzer (303 242 E Artemis, METZSCH, Germany) at room temperature, and then a maximum force of 45 N with a dynamic force of 2.5 N was applied to the sample in the same direction as that of the dynamic nanoindentation analysis test, with a frequency of 1–20 Hz. The results were collated from a minimum of three tests.

Three-point bending test and SENB test

The flexural mechanical properties were analyzed with a Shimadzu AGS-X tester by three-point bending tests and in-situ stretcher (Deben micro-test tensile stage) in Quanta 250 F, FEI. For analysis of samples, a support span of 7.5 mm and a bending displacement rate of 0.1 mm/s were used. The specimens (at least three samples) with a size of 15–20 × 1.2 × 1 mm were cut by a water-cooled, low-speed diamond saw, for three-point bending test. For SENB test, the specimens (at least three samples) with a size of 15–20 × 1.2 × 0.8 mm and a notch length of 0.4-0.6 mm were cut by a water-cooled low-speed diamond saw, the notch was sharpened to width less than 50 µm by using a razor to repeatedly slide and the bending displacement rate is 0.01 mm/min. For the analysis of natural enamel, the specimens were prepared the same as artificial materials (Supplementary Fig. 47), while support span is 2.4 mm and size of the specimens are 3 × 1 × 0.8 mm for three-point bending test and 3 × 1 × 0.8 mm with a notch length of 0.1–0.2 mm for SENB test. And all of the size for samples satisfied the ASTM E1820 standard, including the suggested alternative proportions for the single-edge bending specimen are $1 \le W/B \le 4$, the notch height (N) is $\le 0.063W$, where the sum of the pre-crack extension and the sharpened notch length is $\ge 2\,N$. All specimens for both three-point bending tests and SENB tests were polished by abrasive papers to remove the mechanical damages generated by the cutting process and tested along the direction of perpendicular, longitudinal or transversal to the HA nanowires. It should be noted here that, if there is no special explanation, the flexural strength and toughness are tested along the perpendicular direction to the HA nanowires.

The three-point bending test and SENB test under humid environment were carried out in an environmental chamber with a humidity of 98 %, using the same test method as dry samples.

(1) Calculation of stress (σ)and strain (ε).

According to ASTM D790-03, stress and strain were calculated from the three-point bending force-displacement curves as follows:

$$\sigma = \frac{3FS}{2bd^2} \tag{1}$$

$$\varepsilon = \frac{6Dd}{S^2} \tag{2}$$

where F is the force, D is the displacement and S is the length of support span. b and d represent the specimen width and thickness, respectively. Flexural strength and fracture strain were calculated using the F and D at failure. The stress and strain for SENB samples are calculated from the SENB force-displacement curves according to Eqs. 1 and 2, where the thickness of which is determined as the whole length without deducting the notch.

(2) Calculation of toughness, K_{IC} and K_{JC}[52].

Determination of crack length: the SENB method, using an equivalence between compliance and crack length to obtain crack propagation length, was carried out to analyze the toughness. The compliance was calculated using the relationship $C = \frac{u}{f}$, where u and f represent crack propagation and force at each point after the departure of a crack, respectively. Then the crack length was recursively calculated with:

$$a_n = a_{n-1} + \frac{W - a_{n-1}}{2} \times \frac{C_n - C_{n-1}}{C_n} \tag{3}$$

$$C_n = \frac{u_n}{f_n} \tag{4}$$

$$\Delta \mathrm{a} = a_n - a \tag{5}$$

where W is the width of the sample, a and C are the crack length and compliance, respectively calculated at the n and n-1 step, Δa is the extend amount of crack.

The corroboration of compliance calculation: the compliance and crack length were calculated according to the initial experimental force versus load-line displacement curve by two equations: one is the equations (Eqs. 3 and 4) and the other is equation (Eq. 6) in ASTM E1820 (Supplementary Fig. 48). Whether the values of compliance and crack length obtained by the two kinds of equations are basically consistent is the criterion to finish this corroboration.

$$C_i = \frac{1}{EB_e}\left(\frac{S}{W - a_i}\right) \times \left[1.193 - 1.98\left(\frac{a_i}{W}\right) + 4.478\left(\frac{a_i}{W}\right)^2 - 4.443\left(\frac{a_i}{W}\right)^3 + 1.739\left(\frac{a_i}{W}\right)^4\right] \tag{6}$$

Where $B_e \approx B$, E is Young's modulus, W and B represent the specimen width and thickness, S is the Span of fixture.

K_{IC} was calculated with the following equations:

$$K_{IC} = \frac{P_{ic}S}{BW^{3/2}} f(a/W) \tag{7}$$

$$f\left(\frac{a}{W}\right) = \frac{3(a/W)^{1/2}[1.99 - (a/W)(1 - a/W)(2.15 - \frac{3.39a}{W} + (\frac{a}{W})^2}{2(1 + 2a/W)(1 - a/W)^{3/2}} \tag{8}$$

where P_{ic} is the maximum load value in SENB test, S is support span, B is the thickness, W is the width, a is the initial notch depth of the specimen.

Details on J-integral calculation: Similar assessment methods have been reported previously for natural biological materials and biomimetic composite materials, a J-integral versus crack extension has been calculated as the contribution of elastic and plastic contribution. The elastic contribution, J_{el}, is based on linear-elastic fracture mechanics:

$$J_{el} = \frac{{K_{ic}}^2}{E} \tag{9}$$

$$J_{pl} = \frac{2A_{pl}}{Bb} \tag{10}$$

where A_{pl} represents the plastic area under the load-displacement curve, B represents the specimen lateral dimension, and b represents the un-cracked ligament ($b = W$-a). A geometric mean of the local stress intensity factor leads to an equivalent stress intensity factor:

$$K_{JC} = \sqrt{(J_{el} + J_{pl})E} \tag{11}$$

where K_{JC} is the back-calculated stress intensity factor, J_{el} and J_{pl} are the elastic and plastic contribution of the J-integral, respectively, and E is Young's modulus of composite materials.

$J (J = J_{el} + J_{pl})$ values should be smaller than $B\sigma_y/20$. Also, crack extension lengths below $\Delta a_{\max} = 0.25b$ are considered to be valid.

In order for the J value (or its equivalent K_J value) to be considered as a material property (Jc or K_{JC}), the following criteria need to be met:

$$B > 25J_{\max}/\sigma_y \tag{12}$$

where σ_y is the average of composite's final strengths.

Single-notch cantilever beam tests

The different specimen size of HEA for single-notch cantilever beam tests were cut by FIB (FEI, Helios 600) and conducted in an environmental scanning electron microscope (ESEM) equipped with an in situ mechanical test instrument (Hysitron PI-85) equipped with a flat diamond tip (5 µm in size). During the test, flat tip was pressed against the cantilever from the top with a constant displacement rate of 0.2 μm s^{-1} to initiate cracking from the precut notch. The process of crack propagation was directly observed in the ESEM. The applied load and the testing process were recorded in real-time by the instrument, and the load at fracture P was recorded.

K_{IC} was calculated with the following equations[46]:

$$K_{IC} = F_I \sigma_b \sqrt{\pi a} \tag{13}$$

where F_I are the geometric functions for tension, with the outer fiber tensile stress σ_b given by:

$$\sigma_b = 12\frac{PLp}{BW^2} \tag{14}$$

$$F_I \cong F_{I,rect}\left(1 + 0.87\frac{a}{W}\right) \tag{15}$$

$$F_{I,rect} = \frac{1.1215}{(1-\frac{a}{W})^{3/2}}\left[\frac{5}{8} - \frac{5}{12}\times\frac{a}{W} + \frac{1}{8}\left(\frac{a}{W}\right)^2 + 5\left(\frac{a}{W}\right)^2\left(1-\frac{a}{W}\right)^6 + \frac{3}{8}\exp\left(-6.1342\frac{a}{W}\Big/\left(1-\frac{a}{W}\right)\right)\right] \tag{16}$$

Cyclic contact fatigue test

The contact fatigue tests were conducted using an electro-hydraulic servo fatigue test system at room temperature (Instron, 8872, USA) (See Supplementary Note 6) and the details of these tests were as follows: a shinily spherical aluminum steel contact device (commonly used in contact fatigue tests of tooth) with a radius of 5 mm is applied to finish the contact fatigue test at a frequency of 15 Hz and 1.5 Hz with a sinusoidal force of 0–98 N for 150,000 cycles. It was demonstrated that the load of 98 N is often used to describe the average physiological chewing power of maxillary teeth. Furthermore, the sinusoidal force of 0–98 N is equivalent to the equal effect of oral chewing force in horizontal and vertical directions[53]. Furthermore, research indicates that an individual engages in ~4000 chewing cycles per day, which equals a total of 150,000 cycles per year at a frequency of 1.5 Hz[54]. Hence, the contact loading of samples was conducted in load control at a frequency of 15 Hz with a sinusoidal force of 0–98 N for 150,000 cycles. The samples were cut into a cross-section of 2 mm × 2 mm using a precision slicing machine. Then, the cutting surface was polished by metallographic sandpaper with mesh of #400, #1000, #2000, #3000, and #4000, respectively. After that, the polished samples were embedded vertically in polymethyl methacrylate (PMMA) to a depth of ~5–6 mm. Finally, the examined samples were retrieved for further characterization.

Surface roughness calculation

The arithmetic average of the absolute values of the surface height deviations measured from the mean plane within the box cursor using the equation:

$$\text{Image}R_a = \frac{1}{N}\sum_{j=1}^{N}\left|Z_j\right| \tag{17}$$

where Z_j is the current Z value, and N is the number of points within the box cursor, which in this work equals 65,536.

Toothbrushing wear test

HEA (specimen size: 10 × 2 × 2 mm) was fixed to the surface of each sample bench by a self-curing resin to reach the same exposure height (See Supplementary Note 7). A 200 g load was delivered by soft toothbrushes (Oral-B Indicator 35 Toothbrush, Short Head, UK), and all test samples were immersed in a slurry of toothpaste (Oral-B Pro-Health, Procter & Gamble) solution that comprised 16 g of toothpaste with 100 mL of deionized water. The samples were subjected to a total of 15,000 reciprocal strokes (60 cycles min^{-1}) of toothbrushing (a custom-made machine designed in accordance with ISO/TR 14569-1:2007), which equates to ~1 year of toothbrushing wear. Once the 15,000 stroke mechanical wear tests were complete, the enamel blocks were disassembled from the resin in order to be observed using AFM observation and undergo nanoindentation testing.

Abrasion test

Abrasion test on HEA (specimen size: 10 × 10 × 2 mm) was measured by UMT-5 friction testing machine (Brucker, Germany) equipped with a load of 10–25 N and with a crosshead speed of 70 r/min at the temperature of 36.5 °C.

Shear bond strength test

The rectangle specimens were bonded with Embrace WetBond (3MESPE U200) in enamel slice for the shear bond tests. The shear bond tests were performed at room temperature by applying a load parallel to the interface of samples and enamel at a shear speed of 0.75 ± 0.30 mm/min by using an Instron 5969 50 kN machine (United States). A stainless steel jig was driven to realize the shear test by a stainless steel piston. The shear bond strength ($P = F/S$, MPa) was obtained by the relation between the peak fracture force (F, N) and the contact area of the adherent enamel slice (S, mm^2). The results were statistically analyzed with a significance level of $p < 0.05$ using the SPSS 17.0 software for Windows (Chicago, IL, USA).

Bacterial adhesion test

Candida albicans (ATCC 25175) was purchased from the China General Microbiological Culture Collection Center and cultured in brain-heart infusion medium (Sigma-Aldrich, St. Louis, MO, USA). Enamel and HEA were immersed in distilled water, placed in a 5 ml test tube and subjected to Co 60 radiation sterilization. For the bacterial adhesion testing, the enamel blocks were placed in 48-well plates and pretreated with artificial saliva (A7990, Solarbio, China) for 30 min at 37 °C to mimic the natural oral condition. The optical density of Candida albicans at 530 nm (OD630) was adjusted to 0.02 (~1 × 10^7 CFU/ml), and a 400 μL volume of bacterial suspension was placed onto each enamel surface. To quantify the bacteria adhering to the enamel blocks, samples were removed from the bacterial suspension and rinsed with phosphate-buffered solution (PBS) three times. Samples cultured with Candida albicans at 37 °C for ~1 and 4 h were fixed in 2.5% glutaraldehyde solution, rinsed with distilled water, dehydrated in a graded series of ethanol solutions (50%, 60%, 70%, 80%, 90%, and 100%) for 15 min. They were then observed with SEM. The number of adherent cells in nine randomly selected 5000-fold magnification fields was counted, and the number of bacteria in 1 mm^2 was calculated. After a 12-h incubation period, the antibacterial activity was evaluated using a live/dead assay kit (Invitrogen, Singapore) for 15 min in the absence of light. Subsequently, the samples were imaged using a confocal laser scanning microscope (CLSM) (Carl Zeiss, Jena, Germany). The fluorescence intensity area of layers from 3D images was calculated using Image Pro Plus 6.0.

Biocompatibility property test

The biocompatibility property of the materials was tested by co-culturing with HGF (ScienCel #2620, USA). Cells were cultured with basal alpha modified Eagle's medium (α-MEM) added fetal bovine serum (FBS), 100 × penicillin and streptomycin mixture (Gibco, China). After sterilization, the enamel blocks from different groups were placed in 48-well plates and HGF were seeded at 1.0 × 10^4 cells per well. Cell adhesion was tested by laser confocal microscope. After 1, 3, and 5 days of co-culturing, samples were washed with PBS and fixed in 4% paraformaldehyde for 10 min at room temperature. The samples were washed three times in PBS and postfixed in 0.1% Triton X-100 for 15 min at room temperature. The samples were washed another three times in PBS and then blocked by 3% bovine serum albumin (BSA). Later, the enamel blocks were incubated with 1:200 anti-vinculin primary antibodies (Abcam ab129002, UK) overnight at 4 °C. Samples were washed and incubated in 1:250 anti-rabbit secondary antibodies (Abcam ab150081, UK) for 1 h at room temperature. Then they were washed and incubated in 1:200 TRITC Phalloidin (Solarbio CA1610, China) for 1 h and 5 mg/ml DAPI solution for 10 min at room temperature for marking of cell cytoskeleton and nucleus. The area of the cell was quantified using Image Pro Plus 6.0. The rate of cell proliferation was determined using CCK-8 assay (Dojindo Laboratories, Kumamoto, Japan). The optical density at a wavelength of 450 nm of the formazan dye product in the cultures was measured and recorded. The results were collated from a minimum of three tests for different samples of enamel and HEA, respectively.

Reporting summary

Further information on research design is available in Nature Portfolio Reporting Summary linked to this article.

Data availability

All data generated in this study are provided in the Supplementary Information/Source Data file. Additional raw data are available from the corresponding authors upon request. Source data are provided with this paper. The data used in this study are available in Figshare (https://doi.org/10.6084/m9.figshare.27175068). Source data are provided with this paper.

References

1. Taubman, M. A. & Nash, D. A. The scientific and public-health imperative for a vaccine against dental caries. *Nat. Rev.* **6**, 555–563 (2006).
2. Zhao, H. et al. Multiscale engineered artificial tooth enamel. *Science* **375**, 551–556 (2022).
3. Tan, G. et al. Nature-inspired nacre-like composites combining human tooth-matching elasticity and hardness with exceptional damage tolerance. *Adv. Mater.* **31**, e1904603 (2019).
4. Denry, I. & Kelly, J. R. Emerging ceramic-based materials for dentistry. *J. Dent. Res.* **93**, 1235–1242 (2014).
5. Conrad, H. J. et al. Current ceramic materials and systems with clinical recommendations: a systematic review. *J. Prosthet. Dent.* **98**, 389–404 (2007).
6. Jin, C. X. et al. Comparative study on the impact-sliding wear behaviour of CAD/CAM resin-ceramic materials and tooth enamel. *Dent. Mater.* **39**, 25–40 (2023).
7. Yeom, B. et al. Abiotic tooth enamel. *Nature* **543**, 95–98 (2017).
8. Hannouche, D. et al. Ceramics in total hip replacement. *Clin. Orthop. Relat. Res.* **430**, 62–71 (2005).
9. Zhang, J. et al. Documentation of damping capacity of metallic, ceramic and metal-matrix composite materials. *J. Mater. Sci* **28**, 2395–2404 (1993).
10. Li, Y. et al. Bioprocess-inspired room-temperature synthesis of enamel-like fluorapatite/polymer nanocomposites controlled by magnesium ions. *ACS Appl. Mater. Interfaces* **13**, 25260–25269 (2021).
11. Zhao, H. et al. Natural tooth enamel and its analogs. *Cell Rep. Phys. Sci.* **3**, 100945 (2022).
12. Yu, H.-P. et al. Bioinspired fiberboard-and-mortar structural nanocomposite based on ultralong hydroxyapatite nanowires with high mechanical performance. *Chem. Eng. J.* **399**, 125666 (2020).
13. Li, L. et al. Bio-inspired enamel repair via Glu-directed assembly of apatite nanoparticles: an approach to biomaterials with optimal characteristics. *Adv. Mater.* **23**, 4695–4701 (2011).
14. Wang, D. et al. Controlling enamel remineralization by amyloid-like amelogenin mimics. *Adv. Mater.* **32**, e2002080 (2020).
15. Lawn, B. R. et al. Teeth: among nature's most durable biocomposites. *Ann. Rev. Mater. Res.* **40**, 55–75 (2010).
16. Cuy, J. L. et al. Nanoindentation mapping of the mechanical properties of human molar tooth enamel. *Arch. Oral. Biol.* **47**, 281–291 (2002).
17. Zhang, Y. R. et al. Review of research on the mechanical properties of the human tooth. *Int. J. Sci.* **6**, 61–69 (2014).
18. DeRocher, K. A. et al. Chemical gradients in human enamel crystallites. *Nature* **583**, 66–71 (2020).
19. Yun, F. et al. Nanoscale pathways for human tooth decay—central planar defect, organic-rich precipitate and high-angle grain boundary. *Biomaterials* **235**, 119748 (2020).
20. Thompson, V. P. The tooth: an analogue for biomimetic materials design and processing. *Dent. Mater.* **36**, 25–42 (2020).
21. Koenigswald, W. V. & Clemens, W. Levels of complexity in the microstructure of mammalian enamel and their application in studies of systematics. *Scan. Microsc.* **6**, 195–218 (1992).
22. Bechtle, S. et al. Hierarchical flexural strength of enamel: transition from brittle to damage-tolerant behaviour. *J. R. Soc. Interface* **9**, 1265–1274 (2012).
23. Prasad, V. et al. PET/CT in neuroendocrine tumors: evaluation of receptor status and metabolism. *PET Clin.* **2**, 351–375 (2007).
24. Pasteris, J. D. et al. Bone and tooth mineralization: why apatite? *Elements* **4**, 97–104 (2008).
25. Koldehoff, J. et al. Influence of water and protein content on the creep behavior in dental enamel. *Acta Biomater.* **158**, 393–411 (2023).
26. Chen, J. et al. Biomechanics of oral mucosa. *J. R. Soc. Interface* **12**, 20150325 (2015).
27. He, L. H. et al. Elastic modulus and stress-strain response of human enamel by nano-indentation. *Biomaterials* **27**, 4388–4398 (2006).
28. Rees, J. S. et al. The elastic modulus of dentine determined by static and dynamic methods. *Clin. Mater.* **17**, 11–15 (1994).
29. Lakes, R. S. et al. Extreme damping in composite materials with negativestiffness inclusions. *Nature* **410**, 565–567 (2001).
30. Randall, M. E. et al. Composites reinforced in three dimensions by using low magnetic fields. *Science* **335**, 199–204 (2012).
31. Kajiyama, S. et al. Shear-induced liquid-crystalline phase transition behaviour of colloidal solutions of hydroxyapatite nanorod composites. *Nanoscale* **12**, 11468–11479 (2020).
32. Rees, J. S. et al. The elasti modulus of dentine determineynamic methods. *Clin. Mater.* **17**, 11–15 (1994).
33. Fontijn-Tekamp, F. A. et al. Biting and chewing in overdentures, full dentures, and natural dentitions. *J. Dent. Res.* **79**, 1519–1524 (2000).
34. Gao, S. S. et al. Contact fatigue of human enamel: experiments, mechanisms and modeling. *J. Mech. Behav. Biomed.* **60**, 438–450 (2016).
35. Wang, L. D. et al. Wear resistance of packable resin composites after simulated toothbrushing test. *J. Esthet. Restor. Dent.* **16**, 303–314 (2004).
36. Wei, Y. et al. Enamel repair with amorphous ceramics. *Adv. Mater.* **32**, 1907067 (2020).
37. Gibbons, R. J. Adherent interactions which may affect microbial ecology in the mouth. *Microb. Ecol.* **63**, 378–385 (1984).
38. Wegst, U. G. et al. Bioinspired structural materials. *Nat. Mater.* **14**, 23–36 (2015).
39. Bechtle, S. et al. The fracture behaviour of dental enamel. *Biomaterials* **31**, 375–384 (2010).
40. Bajaj, D. & Arola, D. D. On the R-curve behavior of human tooth enamel. *Biomaterials* **30**, 4037–4046, (2009).
41. Koester, K. J. et al. The effect of aging on crack-growth resistance and toughening mechanisms in human dentin. *Biomaterials* **29**, 1318–1328 (2008).
42. Bouville, F. et al. Strong, tough and stiff bioinspired ceramics from brittle constituents. *Nat. Mater.* **13**, 508–514 (2014).
43. Chen, Y. et al. Artificial wooden nacre: a high specific strength engineering material. *ACS Nano* **14**, 2036–2043 (2020).

44. Chen, Y. et al. Synthesis and properties of Poly(vinyl alcohol) hydrogels with high strength and toughness. *Polym. Test.* **108**, 107516 (2022).
45. Zhang, J. Y. et al. Tough and strong biomimetic soy protein films with excellent UV-shielding performance. *Compos. Part B* **226**, 109379 (2021).
46. Bechtle, S. et al. A method to determine site-specific, anisotropic fracture toughness in biological materials. *Scripta Mater* **66**, 515–518 (2012).
47. Liu, Z. et al. On the materials science of nature's arms race. *Adv. Mater.* **30**, e1705220 (2018).
48. Yang, R. L. et al. Bioinspired macroscopic ribbon fibers with a nacre-mimetic architecture based on highly ordered alignment of ultralong hydroxyapatite nanowires. *ACS Nano* **12**, 12284–12295 (2018).
49. Xu, Z. et al. Ultrastrong fibers assembled from giant graphene oxide sheets. *Adv. Mater.* **25**, 188–193 (2013).
50. Thompson, K. et al. In situ site-specific specimen preparation for atom probe tomography. *Ultramicroscopy* **107**, 131–139 (2007).
51. Oliver, W. C. & Pharr, G. M. An improved technique for determining hardness and elastic modulus using load and displacement sensing indentation experiments. *J. Mater. Res.* **7**, 1564–1583 (1992).
52. Amini, A. et al. Centrifugation and index matching yield a strong and transparent bioinspired nacreous composite. *Science* **373**, 1229–1234 (2021).
53. Giray, F. E. et al. Evaluation of the bond strength of resin cements used to lute ceramics on laser-etched dentin. *Photomed. Laser. Surg.* **32**, 413–421 (2014).
54. Toledano, M. et al. Effect of cyclic loading on the microtensile bond strengths of total-etch and self-etch adhesives. *Oper. Dent.* **31**, 25–32 (2006).
55. Ashby, M. F. Materials Selection in Mechanical Design: Material Property Charts. Ch. 4, 57–95 (Publisher, ed. 4, 2011).
56. Wei, J. J. et al. Bioprocess-inspired microscale additive manufacturing of multilayered TiO_2/polymer composites with enamel-like structures and high mechanical properties. *Adv. Funct. Mater.* **30**, 1904880 (2020).
57. Gabriella, A. C. S. & Ling, Y. Response of pre-crystallized CAD/CAM zirconia-reinforced lithium silicateglass ceramic to cyclic nanoindentation. *J. Mech. Behav. Biomed.* **92**, 58–70 (2019).
58. Yan, S. G. et al. A comparative study on the microscale and macroscale mechanical properties of dental resin composites. *Polymers* **15**, 1129 (2023).
59. Yan, W. Y. et al. On anomalous depth-dependency of the hardness of NiTi shape memory alloys in spherical nanoindentation. *J. Mater. Res.* **28**, 2031–2039 (2013).
60. Peskersoy, C. & Sahan, H. M. Finite element analysis and nanomechanical properties of composite and ceramic dental onlays. *Comput. Method. Biomec.* **25**, 1649–1661 (2022).
61. Woigk, W. et al. Bio-inspired platelet-reinforced polymers with enhanced stiffness and damping behavior. *ACS Appl. Polym. Mater.* **2**, 3557–3565 (2020).
62. Lakes, R. S. High damping composite materials: effect of structural hierarchy. *J. Compos. Mater.* **36**, 287–297 (2002).
63. Lakes, R. S. Extreme damping in composite materials with a negative stiffness phase. *Phys. Rev. Lett.* **86**, 2897 (2001).
64. Wegst, U. G. K. & Ashby, M. F. The mechanical efficiency of natural materials. *Philos. Mag.* **84**, 2167–2186 (2004).
65. Yu, Y. et al. Studies on dynamic mechanical and electrical properties of PZT ceramics. *Ferroelectrics* **451**, 96–102 (2013).
66. Chow, W. et al. Mechanical and thermal properties of hydroxyapatite filled poly (methyl methacrylate) composites. *Proc. Polym. Process. Soc.* **24**, 15–19 (2008).
67. Shen, Z. et al. Dense hydroxyapatite–zirconia ceramic composites with high strength for biological applications. *Adv. Mater.* **13**, 214–216 (2001).
68. Kim, S. et al. Effect of calcinations of starting powder on mechanical properties of hydroxyapatite-alumina bioceramic composite. *J. Mater. Sci. Mater. Med.* **13**, 307–310 (2002).
69. Nie, J. et al. Effect of TiO_2 doping on densification and mechanical properties of hydroxyapatite by microwave sintering. *Ceram. Int.* **45**, 13647–13655 (2019).
70. Aguirre, T. G. et al. Effects of the addition of boron nitride nanoplate on the fracture toughness, flexural strength, and weibull distribution of hydroxyapatite composites prepared by spark plasma sintering. *J. Mech. Behav. Biomed. Mater.* **93**, 105–117 (2019).
71. Takeoka, Y. et al. In situ preparation of poly (l-lactic acid-co-glycolic acid)/hydroxyapatite composites as artificial bone materials. *Polym. J.* **47**, 164–170 (2015).
72. Ravikumar, K. et al. Twinning induced enhancement of fracture toughness in ultrafine-grained hydroxyapatite–calcium titanate composites. *J. Eur. Ceram. Soc.* **36**, 805–815 (2016).
73. Kumar, A. et al. On the toughness enhancement in hydroxyapatite-based composites. *Acta Mater* **61**, 5198–5215 (2013).
74. Li, A. et al. Mechanical properties, microstructure and histocompatibility of MWCNTs/HAp biocomposites. *Mater. Lett.* **61**, 1839–1844 (2007).
75. Zhang, H. & Darvell, B. W. Mechanical properties of hydroxyapatite whisker-reinforced bis-GMA-based resin composites. *Dent. Mater.* **28**, 824–830 (2012).
76. Dirks, J. & Taylor, H. D. Fracture toughness of locust cuticle. *J. Exp. Biol.* **215**, 1502–1508 (2012).
77. Munch, E. et al. Tough, bio-inspired hybrid materials. *Science* **322**, 1516–1520 (2008).
78. Low, I. M. et al. Mechanical and fracture properties of bamboo. *Key Eng. Mater.* **312**, 15–20 (2006).
79. Prokopski, G. The application of fracture mechanics to the testing of wood. *J. Mater. Sci.* **28**, 5995–5999 (1993).
80. Melnick, C. et al. Hardness and toughness of exoskeleton material in the stone crab, Menippe mercenaria. *J. Mater. Res.* **11**, 2903–2907 (1996).
81. Clifton, K. et al. Material properties of manatee rib bone. *J. Zool.* **274**, 150–159 (2008).
82. Gao, H. L. et al. Mass production of bulk artificial nacre with excellent mechanical properties. *Nat. Commun.* **8**, 287 (2017).
83. Bai, H. et al. Bioinspired hydroxyapatite/poly(methyl methacrylate) composite with a nacre-mimetic architecture by a bidirectional freezing method. *Adv. Mater.* **28**, 50–56 (2016).
84. Martin, J. J. et al. Designing bioinspired composite reinforcement architectures via 3D magnetic printing. *Nat. Commun.* **6**, 8641 (2015).
85. Mao, L. B. et al. Synthetic nacre by predesigned matrix-directed mineralization. *Science* **354**, 107–110 (2016).
86. Liu, Z. Q. et al. On the materials science of nature's arms race. *Adv. Mater.* **30**, 1705220 (2018).
87. Studart, A. R. et al. Towards high-performance bioinspired composites. *Adv. Mater.* **24**, 5024–5044 (2012).

Acknowledgements

We thank Peking University School and the Hospital of Stomatology for providing natural tooth enamel. This work was supported by the National Key R&D Program of China (2020YFA0710403), the National Natural Science Foundation of China (52222203, 52073008, 52250119, 52102086), and the Beijing Municipal Science & Technology Commission (221100007422088).

Author contributions

L.G., H.Z., L.J., and X.D. conceived this project. J.L., Q.Z., S.L., F.L., and Y.L. synthesized the hierarchical tooth analogs. H.Z., J.L., and S.L. carried out morphology, structure, and mechanical analysis of HEA. X.D., Y.W., and J.D. performed the biology analysis of HEA. L.G., H.Z., L.J., J.L., and

X.Y. wrote this paper. All authors participated in the discussions of this study.

Competing interests

The authors declare no competing interests.

Additional information

Supplementary information The online version contains supplementary material available at https://doi.org/10.1038/s41467-024-54576-5.

Correspondence and requests for materials should be addressed to Hewei Zhao, Xuliang Deng, Lei Jiang or Lin Guo.

Peer review information *Nature Communications* thanks Renan Belli and the other, anonymous, reviewer(s) for their contribution to the peer review of this work. A peer review file is available.

Reprints and permissions information is available at http://www.nature.com/reprints

Publisher's note Springer Nature remains neutral with regard to jurisdictional claims in published maps and institutional affiliations.

Open Access This article is licensed under a Creative Commons Attribution-NonCommercial-NoDerivatives 4.0 International License, which permits any non-commercial use, sharing, distribution and reproduction in any medium or format, as long as you give appropriate credit to the original author(s) and the source, provide a link to the Creative Commons licence, and indicate if you modified the licensed material. You do not have permission under this licence to share adapted material derived from this article or parts of it. The images or other third party material in this article are included in the article's Creative Commons licence, unless indicated otherwise in a credit line to the material. If material is not included in the article's Creative Commons licence and your intended use is not permitted by statutory regulation or exceeds the permitted use, you will need to obtain permission directly from the copyright holder. To view a copy of this licence, visit http://creativecommons.org/licenses/by-nc-nd/4.0/.

© The Author(s) 2024